J. Fluid Mech. (2007), *vol.* 578, *pp.* 467–494.
doi:10.1017/S0022112007005368 Printed in the United Kingdom

The development of the turbulent flow in a bent pipe

PHILLIP L. WILSON[1] AND FRANK T. SMITH[2]

[1]Department of Mathematics & Statistics, University of Canterbury, Private Bag 4800, Christchurch 8140, New Zealand

[2]Department of Mathematics, University College London, Gower Street, London, WC1E 6BT, UK

(Received 2 November 2005 and in revised form 8 December 2006)

The three-dimensional incompressible turbulent flow through a slender bent pipe of simple cross-section is analysed, the pipe gradually bending the rapid flow through a substantial angle. The ratio of the relative radius of curvature to the magnitude of the turbulent fluctuations is crucial: analysis of the entry region involving exact solutions of the governing equations shows three different downstream developments, depending on the magnitude of that ratio. The main velocity components are found in each case, and one downstream development studied in detail is when turbulence dominates the flow.

The main novel points and results are as follows. (i) The present physical situation which arises commonly in industrial settings has been little studied previously by theory or experiments. (ii) The working applies for any two-tier mixing-length model. (iii) As a most surprising feature, the fully developed flow far downstream is not unique, being found to depend instead on the global flow behaviour (thus the centreline velocity is not determined simply by the pressure drop, in contrast to the laminar case). (iv) A quite accurate predictive tool based on approximation is suggested for the downstream flow. (v) Crossflow maxima are found to occur very close to the walls, as observed in experiments. (vi) Other comparisons are made with experimental data and prove generally favourable.

1. Introduction

This work on the three-dimensional turbulent flow in a bent pipe arises from investigations on rapid flow through such pipes in an industrial application. A major type of food-sorting machine (see Smith & Li 2002) has air guns connected to an air source pressurized to 2–6 atm, depending on application. Millisecond pulses of air pass rapidly through an air gun, whose interior geometry may typically include a long straight section joined without smoothing to a bent section. The bend has a representative turning angle of 90° and is of moderate curvature; the characteristic ratio ϵ of the pipe cross-sectional width to the radius of curvature of the pipe centreline is $O(10^{-1})$. Typical flow Reynolds numbers are $O(10^5)$, based on the pipe cross-sectional width.

The short duration and large Reynolds number point to a nonlinear and inviscid treatment of the three-dimensional core flow (Smith & Li 2002; Wilson 2003; Wilson & Smith 2005*b*), apart from over a short length scale close to the start of the bend as in Wilson & Smith (2005*a*). Moreover, the increased likelihood of turbulent effects

due to unavoidable manufacturing defects for example motivates the present study of the development of the contained turbulent motion, including entry wall layers (wall roughness effects and the transition to turbulence are not explicitly studied here).

We study the three-dimensional growth and development of the turbulent flow in a bent pipe of simple cross-section. The analysis here involves theoretical and numerical approaches, and comparisons are made with experimental data from the literature. There appear to be few empirical data for turbulent wall layers in pipes with the particular level of curvature assumed in this paper. A single example is in Ellis & Joubert (1974), but the experiment there involved a rectangular pipe with aspect ratio over 13 (an order of magnitude larger than for the pipe we consider here) which effectively excludes any secondary flow in the cross-section. Furthermore, measurements are made only further downstream than we consider. As a result, no comparisons with the data in that study can be made.

The apparent lack of empirical work for turbulent flows in pipes with the curvature considered herein may be due to this curvature lying somewhere between strongly bent, such as an elbow, and weakly bent, several orders of magnitude weaker than the strong case. Experiments in these two regimes include Schwarz & Bradshaw (1994) in the first instance, and Hunt & Joubert (1979) in the second. However, the present theoretical study is aimed less at confirming experimental results or proving the utility of a particular model than at investigating the physical situation which commonly arises in industrial settings. In contrast to the measuring of higher-order statistical quantities, or coherent and transient structures, the present study is largely concerned with the development of velocity and pressure profiles, and how these influence the core flow, since it is the bulk behaviour of the whole pipe flow which is of importance to the motivating industrial problem.

In the entry region at the start of the bend considered in § 2, both turbulent effects in the boundary-layer (wall-layer) flow and the swirl in the core flow are equally significant. Importantly, the analysis holds for any two-tier mixing-length model of the eddy viscosity, although we select the Cebeci–Smith model (see e.g. Cebeci & Smith 1974) in order to obtain quantitative solutions. A crucial balance (ratio) β of the initially small turbulent and swirl effects enables an exact solution to the entry region equations to be found in § 3. Indeed, varying β describes three different downstream developments. In § 4, a similarity solution is found for the main streamwise velocity term, and a combined similarity and numerical solution found for the main crossflow velocity term. The crossflow involves an adjustment to the wall conditions over an unusually short distance.

A turbulence-dominated pipe is one far-downstream evolution which is studied in § 5 in detail because it is readily realizable in practical terms. In both two and three dimensions, our analysis shows that the pipe centreline velocity is an important parameter governing the entire flow solution and yet, unlike in laminar flow, cannot be derived simply by knowledge of the pressure drop in the pipe. Surprisingly, therefore, the turbulent fully developed flow solution far downstream is found to depend on the flow behaviour globally, i.e. on the complete flow development beforehand. Numerical solutions indicate that both the pipe centreline velocity and the position of the junction between the two layers of the contained flow initially grow linearly in agreement with predictions from an asymptotic analysis at small downstream distances. When close to the pipe centreline, however, the centreline velocity and junction position adjust smoothly and quickly to new invariant values. We confirm this behaviour with an analysis based on neglecting the outer part of the turbulent stress model, giving a useful predictive tool. Comparisons are made with reported experimental work.

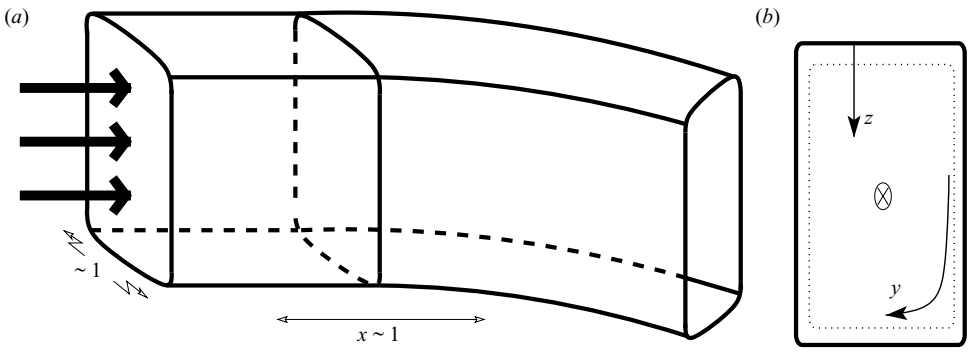

FIGURE 1. Non-dimensional coordinate configuration. (In a dimensional picture the length labelled ~ 1 under the thick arrows would be replaced by h_D.) The thin dotted line in (*b*) indicates the boundary layer.

Finally, in § 6 we demonstrate that the derived results are consistent with Fanno flow (see e.g. Knight 1998), in that the wall frictional effects can be modelled rationally by the mean influences of the growth of the turbulent wall layer, and § 7 presents further comments.

2. The three-dimensional entry behaviour and the parameter β

Turbulent wall layers have inner and outer tiers whose flows merge via a thin logarithmic layer. Analytically, the two-tiered structure emerges for large Reynolds number (Bush & Fendell 1972; Mellor 1972; Sychev 1987; Degani, Smith & Walker 1993). In this paper, we consider two-tier models in which the main balance of forces in the outer layer is between inertia and turbulence, while that in the inner layer is between turbulent and laminar viscous stresses. The inner and outer velocities and eddy viscosity are smoothly joined between the two tiers. We use the Cebeci–Smith model (Cebeci & Smith 1974) of the eddy viscosity, which is perhaps the simplest of the various two-tier models, but it is important to remark that our results are valid for any two-tier mixing-length model. The following sub-sections tackle the governing equations, inlet flow in a straight or bent pipe, and the swirl–turbulence balance, in turn.

2.1. *Governing equations*

The flow is taken to be steady and incompressible, with inertia terms dominating the core flow. Lengths are non-dimensionalized on the representative pipe width h_D, velocities on the typical pipe centreline velocity $U_{D\infty}$, pressure and the Reynolds stresses on $\rho_D U_{D\infty}^2$, and the laminar stresses on $\mu_D U_{D\infty}/h_D$. The Reynolds number is $Re = (\rho_D U_{D\infty} h_D)/(\mu_D)$.

The pipe lies at rest such that the bulk flow is in a horizontal direction, with two non-dimensional coordinate directions (x, y) in the wall and one (z) normal to the wall (figure 1) and corresponding non-dimensional velocities (u, v, w) which represent components of the mean velocity. On a boundary-layer length scale, z is 'short'. The interior surface is regular and away from the corners has small curvature compared to the wall-layer thickness. The non-dimensional length functions are h_1, h_2, h_3, with h_3 being unity (Mager 1964), and the non-dimensional curvature K_1 measures the rate of change with x of the pipe circumference, while non-dimensional curvature K_2 measures the streamwise curvature of the pipe. The non-dimensional continuity and

Navier–Stokes equations are then

$$\frac{1}{h_1}\frac{\partial u}{\partial x}+\frac{1}{h_2}\frac{\partial v}{\partial y}+\frac{\partial w}{\partial z}-K_1u-K_2v=0, \tag{2.1a}$$

$$\frac{u}{h_1}\frac{\partial u}{\partial x}+\frac{v}{h_2}\frac{\partial u}{\partial y}+w\frac{\partial u}{\partial z}-K_2uv+K_1v^2=-\frac{1}{h_1}\frac{\partial p}{\partial x}+\frac{1}{Re}\frac{\partial^2 u}{\partial z^2}+\frac{\partial}{\partial z}\left(B\frac{\partial u}{\partial z}\right), \tag{2.1b}$$

$$\frac{u}{h_1}\frac{\partial v}{\partial x}+\frac{v}{h_2}\frac{\partial v}{\partial y}+w\frac{\partial v}{\partial z}-K_1uv+K_2u^2=-\frac{1}{h_2}\frac{\partial p}{\partial y}+\frac{1}{Re}\frac{\partial^2 v}{\partial z^2}+\frac{\partial}{\partial z}\left(B\frac{\partial v}{\partial z}\right), \tag{2.1c}$$

where we have assumed that the eddy viscosity is isotropic and given by

$$B=\begin{cases} a_2z^2\left[1-\exp\left(-\dfrac{Re^{1/2}}{26}z\left[\left(\dfrac{\partial u}{\partial z}\right)^2_{wall}+\left(\dfrac{\partial v}{\partial z}\right)^2_{wall}\right]^{1/4}\right)\right]^2 \\ \qquad\qquad \times\left[\left(\dfrac{\partial u}{\partial z}\right)^2+\left(\dfrac{\partial v}{\partial z}\right)^2\right]^{1/2}, & z<z_J, \\ a_1u_t\delta_1, & z>z_J, \end{cases} \tag{2.2}$$

$$\delta_1=\int_0^{z_e}1-\frac{(u^2+v^2)^{1/2}}{u_t}\,\mathrm{d}z, \quad u_t=(u^2+v^2)^{1/2}|_{z=z_e}. \tag{2.3}$$

Here (see Nikuradse 1933; Klebanoff 1954; Cebeci & Smith 1974; Neish & Smith 1988) $a_1=0.0168$ is an experimental constant, $a_2=0.16$, z_J is the unknown junction between the layers, and δ_1 is the displacement thickness, a measure of the distance by which streamlines are displaced due to the presence of the wall layer. The model splits each velocity component into a mass-weighted average part (components u, v, w above) and a fluctuating part. The averaged quantities are the solutions to the above equations, and the extra terms introduced by the fluctuating components are responsible for the turbulent transport of momentum and other quantities. This transport process is similar to the molecular transport of Newtonian viscosity, and thus the turbulent (Reynolds) stresses are modelled by analogy with the laminar (Newtonian) stresses as being proportional to a velocity gradient. This introduces the variable coefficient of turbulent viscosity called the eddy viscosity, B. The boundary conditions are for no slip at the walls,

$$\boldsymbol{u}=(u,v,w)\equiv\boldsymbol{0} \quad \text{on } z=0, \tag{2.4a}$$

$$\text{non-wall stresses to be zero at } z=0, \text{ all stresses to be zero at } z\geqslant z_e, \tag{2.4b}$$

where z_e is the location of the edge of the wall layer; and for the boundary-layer flow to match with the core flow at the layer edge,

$$(u,v)=(u_\infty,v_\infty) \text{ at } z=z_e, \tag{2.4c}$$

where (u_∞,v_∞) are the streamwise and crossflow velocities in the core. We also require continuity of the eddy viscosity B, the velocity components u, v, and the shears $\partial u/\partial z$, $\partial v/\partial z$ across $z=z_J$.

In all the subsequent work we assume a pipe of constant cross-sectional area, such that K_1 is zero. The effects of sudden changes in cross-sectional area are considered in Nakao (1986). The present task is to solve (2.1a)–(2.4c) for the unknowns u, v, w, p.

2.2. *Inlet flow in a straight pipe*

For zero K_2, a flow solution is $v \equiv 0$, $p = p(x)$: in a straight pipe, the turbulent wall layers are two-dimensional. The wall layers act as if planar because they lie relatively close to the walls, except possibly near any corners. More formally, a straight, constant cross-section pipe with inlet flow has K_1, K_2, v zero, h_1, h_2, h_3 unity, and p known. Asymptotically (Bush & Fendell 1972; Mellor 1972), the outer tier has thickness $O(\hat{\epsilon})$, for $\hat{\epsilon} \equiv (\ln(Re))^{-1} \ll 1$, with a deficit from free-stream velocity also $O(\hat{\epsilon})$, while the inner tier is $O(Re^{-1}\hat{\epsilon}^{-1})$ thick with u now of $O(\hat{\epsilon})$. The major balance of forces in the outer tier is between inertia and the Reynolds stresses, and the outer tier contains the junction position z_J. Following Bush & Fendell (1972), Mellor (1972) and Neish & Smith (1988), we expand as follows: $u \sim 1 + \hat{\epsilon}u_1 + \hat{\epsilon}^2(\ln(\hat{\epsilon}))u_{2L} + \hat{\epsilon}^2 u_2$; $w \sim \hat{\epsilon}^2 w_1 + \hat{\epsilon}^3(\ln(\hat{\epsilon}))w_{2L}$. The expansion for w comes from the continuity balance, after setting $z = \hat{\epsilon}\bar{z}$ where $\bar{z}$ is $O(1)$. This allows the displacement thickness to be found to leading order, but for higher-order determination of the flow field and displacement thickness, z_J should also be expanded asymptotically. These expansions and length scales suggest that δ_1 is $O(\hat{\epsilon}^2)$, and we take $\delta_1 \sim \hat{\epsilon}^2\hat{\delta}_1 + \hat{\epsilon}^3(\ln(\hat{\epsilon}))\hat{\delta}_{2L} + \hat{\epsilon}^3\hat{\delta}_2$.

Under inlet conditions, the only change in pressure comes about locally owing to an external displacement of the potential flow field. Since the slope of the turbulent wall layer is $O(\hat{\epsilon}^2)$, the external induced pressure near the edge must be $O(\hat{\epsilon}^2)$, and this is also the size of the internal flow field pressure. Hence, $p \sim \hat{\epsilon}^2 p_1$. The dominant balance of the x-momentum equation is:

$$\frac{\partial u_1}{\partial \bar{z}} = \begin{cases} a_2 \dfrac{\partial}{\partial \bar{z}}\left(\bar{z}^2\left(\dfrac{\partial u_1}{\partial \bar{z}}\right)^2\right) & \text{for } \bar{z} < \bar{z}_J, \\ a_1\hat{\delta}_1 \dfrac{\partial^2 u_1}{\partial \bar{z}} & \text{for } \bar{z} > \bar{z}_J. \end{cases} \tag{2.5}$$

Apart from a difference in normalizing, (2.5) is the same as Neish & Smith's (3.3*b*), and thus $\hat{\delta}_1 \propto x$. Therefore, we can suppose that the turbulent wall layer will grow to fill the pipe by a downstream distance of $O(\hat{\epsilon}^{-2})$.

Straight pipe inlet flow and the flow over an aligned flat plate correspond because of the simplicity of the pipe cross-section and its straightness, giving length functions as all identically unity. The same is not true of a bent pipe. Interaction with the external flow will happen earlier than for a flat plate, as effectively any edge effects from core turbulence, or centrifuging, etc. are amplified as the layers thicken towards the centre of the pipe (see e.g. Schlichting & Gersten 2000; Talbot & Wong 1982).

2.3. *Entry behaviour in a bent pipe*

The shortest notable entry region of a bent pipe occurs over streamwise length scales of order unity, as might be expected, and involves a short-range upstream influence smoothing the incident pressures and velocities across the sudden onset of the bend, quantitatively as described in Wilson & Smith (2005*a*). The present longer-range analysis deliberately omits that upstream influence because our concern is with the flow properties relatively far downstream (at large x) on the short length scale. A constant regular cross-section with zero K_1 ensures that $h_2 = h_2(y)$ only. However, zero v is no longer a solution when K_2 is non-zero, as pipe curvature induces three-dimensional flow in the turbulent wall layers.

The central issues now stem from the matching with the core flow, at large $\bar{z} = \hat{\epsilon}^{-1}z$ in the wall layer. The streamwise flow in the core is of the form $1 + \epsilon U$, where the correction velocity U is independent of x, whereas the swirl in the y-direction is $O(\epsilon^2)$

as the present stage is downstream of the smooth shorter-range pressure and velocity adjustments just mentioned. These core velocities match with the flow over the longer length scale of Smith & Li (2002) and Wilson (2003).

2.4. *The swirl–turbulence balance* β

With $\hat{\epsilon}$ ($\equiv (\ln(Re))^{-1}$) and ϵ (a swirl parameter) taken as having the same order of magnitude for the sake of comparison of their effects, uniform streamwise flow is disturbed in the wall layer in the form: $u \sim 1+\hat{\epsilon}\hat{u}$; $v \sim \hat{\epsilon}^2\hat{v}$; $w \sim \hat{\epsilon}^2\hat{w}$. The small deficit in u is as usual in a turbulent layer, the $O(\hat{\epsilon}^2)$ magnitude of the swirl follows from that of the external swirl, while the magnitude of w stems from the mass conservation.

Normally at large $\bar{z}$ we have $v \to v_\infty$, a core flow velocity contribution which is $O(\epsilon^2)$ as just described, taking the form $v_\infty \sim \epsilon^2 V$. Thus,

$$\hat{v} \to \beta^2 V \quad \text{where} \quad \beta = \hat{\epsilon}^{-1}\epsilon. \tag{2.6}$$

The balancing parameter β in the matching of the wall-layer velocities with the core flow is vital to the flow development in the bent pipe, leading to quantitatively different behaviour depending on its magnitude. Respective typical values of ϵ and $\hat{\epsilon}$ in the background industrial setting are about 0.1 (as mentioned earlier) and 0.2.

Since K_1 is zero, y is a geodesic and the lines of x are the geodesic parallels of y. Now a theorem of Gauss (see Mager 1964, p. 293) yields h_2 unity, as well as h_3 and also we have $K_2 = \epsilon\hat{K}_2$ for consistency with the motivating physical problem, which suggests that $h_1 = 1+\epsilon\bar{h}_1$. In this way $\hat{K}_2 = -\partial\bar{h}_1/\partial y$, and h_1 is absent from the leading-order equations. The main balance of (2.1*a*) is then

$$\frac{\partial\hat{u}}{\partial x} + \frac{\partial\hat{w}}{\partial\bar{z}} = 0. \tag{2.7}$$

Considering the x-momentum equation (2.1*b*), we assume that $\partial u/\partial y \ll \hat{\epsilon}^{-1}$ in keeping with the nature of the cross-section, and we allow the pressure gradient to be retained. The eddy viscosity B must be $O(\hat{\epsilon}^2)$ to balance the dominant inertia term, and the main balance of the x-momentum equation is then between inertial, pressure-gradient and turbulent-stress forces.

All stresses vanish in the core flow, however, giving $-\partial p/\partial x = \partial\hat{u}_e/\partial x$, and the right-hand side here is zero in the entry region because the streamwise core flow is independent of x, leaving

$$\frac{\partial\hat{u}}{\partial x} = \begin{cases} a_2\dfrac{\partial}{\partial\bar{z}}\left(\bar{z}\dfrac{\partial\hat{u}}{\partial\bar{z}}\right)^2, & \bar{z} < \bar{z}_J, \\ a_1\hat{\delta}_1\dfrac{\partial^2\hat{u}}{\partial\bar{z}^2}, & \bar{z} > \bar{z}_J, \end{cases} \tag{2.8}$$

with the pressure gradient exerting no influence. The y-momentum balance retains the K_2u^2 term to leading order. This complication is overcome by the inclusion of a suitable pressure term as examination suggests that the pressure gradient in the y-direction must be $O(\hat{\epsilon}^2)$. Since $\bar{h}_1 = \bar{h}_1(y)$ only, the pressure is $p = \hat{p}_0 + \hat{\epsilon}\hat{p}_1(x) + \epsilon\bar{h}_1 + \hat{\epsilon}^2\hat{p}_2(x, y) + \ldots$, where the constant $\hat{p}_0$ is known from the straight section upstream, and $\mathrm{d}\hat{p}_1/\mathrm{d}x$, $\partial\hat{u}_e/\partial x$ are zero. Furthermore, $-\partial\hat{p}_2/\partial y = \partial\hat{v}_e/\partial x + 2\beta\hat{K}_2\hat{u}_e$, and we note the explicit appearance of β and its implicit influence in both terms involving edge

values. The y-momentum balance becomes

$$\frac{\partial \hat{v}}{\partial x} + 2\beta \hat{K}_2 \hat{u} = \left(\frac{\partial \hat{v}_e}{\partial x} + 2\beta \hat{K}_2 \hat{u}_e \right) + \begin{cases} a_2 \dfrac{\partial}{\partial \bar{z}} \left(\bar{z}^2 \dfrac{\partial \hat{u}}{\partial \bar{z}} \dfrac{\partial \hat{v}}{\partial \bar{z}} \right), & \bar{z} < \bar{z}_J, \\ a_1 \hat{\delta}_1 \dfrac{\partial^2 \hat{v}}{\partial \bar{z}^2}, & \bar{z} > \bar{z}_J. \end{cases} \tag{2.9}$$

The governing equations thus become quasi-two-dimensional; (2.8) gives $\hat{u}$, then (2.9) gives $\hat{v}$ with known $\hat{u}$, consistent with the crossflow being an order of magnitude smaller than the main flow, and finally the continuity equation (2.7) gives $\hat{w}$. However, the appearance of β in the equations, its hidden influence through the pressure gradients, and (2.6), point to the existence of at least three regimes of interest: $\beta \ll 1$; $\beta \sim 1$; and $\beta \gg 1$. Exact solutions below, cover all three different regimes in the entry region.

3. Turbulent versus swirl effects

This section considers the so-called β-split concerned with the above two effects, then the mechanics and analysis involved, and finally the influence on downstream behaviour.

3.1. *The two effects*

The β-split describes the following which we will show is the only (and exact) solution of (2.8), (2.9),

$$\hat{u} = \beta \tilde{u} + 1 \times \tilde{\tilde{u}}, \quad \hat{v} = \beta^2 \tilde{v} + \beta \tilde{\tilde{v}}. \tag{3.1a, b}$$

Here, the tilded quantities are independent of β. The successive terms on the right-hand side in (3.1a) correspond to two influences, swirl and turbulence, respectively, and the working below simply amounts to taking the two effects together. Then, $\tilde{\tilde{u}}, \tilde{\tilde{v}} \to 0$ as $\bar{z} \to \infty$ such that the upper boundary conditions on $\hat{u}, \hat{v}$ are satisfied by $\tilde{u}, \tilde{v}$. That is, $\hat{u}_e = \beta \tilde{u}|_{\bar{z} \to \infty}$, and similarly for $\hat{v}_e$. However, $\hat{u}_e = \beta U_{wall}$ such that the edge value of $\tilde{u}$ identifies naturally with U_{wall}, and similarly for $\tilde{v}$ and V. Furthermore, $\tilde{\tilde{u}}, \tilde{\tilde{v}}$ accommodate the lower boundary conditions, as discussed below.

The β-split emerges naturally from the matching of $\hat{u}, \hat{v}$ with the core flow. At the edge, $\hat{u} \sim \beta$ and is a function of y only there, by the nature of the core flow; but $\hat{u}$ must also have an $O(1)$ component to account for the lower boundary condition on u of no slip. Similarly, (2.9) indicates that $\hat{v}$ is driven by an $O(\beta^2)$ term and an $O(\beta)$ term, prompting the form of (3.1b). The following simplification for (3.1a, b) is seen to work,

$$\tilde{u} \equiv \tilde{u}_e, \quad \tilde{v} \equiv \tilde{v}_e, \tag{3.2a, b}$$

and is justified shortly. Thus the swirl effects $\tilde{u}, \tilde{v}$ are independent of $\bar{z}$, and there remain only the variables $\tilde{\tilde{u}}, \tilde{\tilde{v}}$ to solve for.

3.2. *The mechanics of (3.2a, b)*

Appendix A establishes that throughout the outer layer, $\tilde{u}, \tilde{v}$ simply retain their edge values – where they identify exactly with the values of the core flow at the wall – and we only have to solve for $\tilde{\tilde{u}}, \tilde{\tilde{v}}$. The main factor β disappears from the equations, as do the pressure terms; the matching with the core is accommodated; the lower boundary conditions are considered shortly; and the presence of a contribution in $\hat{K}_2$ makes $\tilde{\tilde{v}}$ non-zero. The β-split is also confirmed by the work in § 4.

3.3. *Further analysis*

We turn now to the lower boundary conditions. As $\bar{z} \to 0$, the inertia and pressure terms are small in comparison with the turbulent stress terms, giving the near-wall asymptote $\hat{u} \sim c_3 \ln(\bar{z}) + k_1(x, y)$, where c_3 is unity so that as the inner tier is entered the main identically unity part of the velocity expansion is cancelled, while the unknown deficit function k_1 of $O(1)$ is determined in the inner tier. Next, in (2.9) the centrifuging term also remains, yielding $\hat{v} \sim 2\hat{K}_2 a_2^{-1}((\bar{z} + c_4)\ln(\bar{z}) + (d_1 - 2)\bar{z} + d_2)$, involving the unknown constants c_4, d_1, d_2. Then the asymptote for $\tilde{\tilde{u}}$ is

$$\tilde{\tilde{u}} \sim \ln(\bar{z}) + k_1(x, y) - \beta U_{wall}(y), \tag{3.3}$$

and similarly for $\tilde{\tilde{v}}$ is

$$\tilde{\tilde{v}} \sim \frac{2\hat{K}_2}{a_2}\bar{z}\ln(\bar{z}) + k_2(x, y) - \beta^2 V_{wall}. \tag{3.4}$$

The interpretation is that the $O(1)$ deficit functions k_i are influenced by the edge values, and then in turn influence the inner tier when it is examined on a smaller normal scale. This suggests that there will be some edge effects, y-dependence, and some cancelling of the edge values much closer to the wall. The inner tier has been shown elsewhere to be more sensitive to external influences (see e.g. Huffman & Bradshaw 1972).

The spatial growth rate of the layer is measured by $\hat{\delta}_1$:

$$\hat{\delta}_1 = \int_0^\infty (-\tilde{\tilde{u}})\,\mathrm{d}\bar{z} \sim a_2 x, \tag{3.5}$$

using (3.3).

3.4. *How β influences the downstream development*

The full solutions given by the β-split (3.1a, b) depend on the size of β, yielding three interpretations in the entry region, and three distinct regimes far downstream.

(i) If $\beta \ll 1$, the solutions of (A 1) and (A 4) dominate, and the edge effects are weak since the curvature-induced swirl is weak in comparison to the magnitude of the turbulent fluctuations. The scalings in (3.1a, b) ensure that the curvature drives only a relatively small cross-flow. The result (3.5) suggests that a new stage develops at a distance $\hat{\epsilon}^{-1}$ ($\ll \epsilon^{-1}$) at which the turbulent wall layer grows to fill the pipe. This merged or merging case is the subject of the investigation in § 5.

(ii) If $\beta \sim 1$, both curvature and turbulence are important and the flow behaviour in the entry region depends on the full solution (3.1) and on the $\bar{z}$-independent core terms carried down from the edges. There is a new stage for $\hat{\epsilon}^{-1} \sim \epsilon^{-1}$ where interaction of the boundary layer and the core occurs. At this stage, an amendment to the Cebeci–Smith model must be considered in order to account for the interaction and the influence of the curvature on the new length scale.

(iii) If $\beta \gg 1$, the core flow dominates the turbulent flow solutions, which is consistent with the interpretation that then the turbulence is weak. There is a new stage at a distance ϵ^{-1} ($\ll \hat{\epsilon}^{-1}$) at which the core becomes fully developed but the wall layer remains thin. In this case, there is no real impact on the core flow results of Smith & Li (2002) since the boundary layer is thin throughout the bend.

Swirl effects become more substantial downstream, rendering the core nonlinear when x becomes $O(\epsilon^{-1})$, whereas turbulent effects alter the whole downstream flow by filling the pipe at a distance $O(\hat{\epsilon}^{-1})$. Swirl dominance thus happens if $\epsilon \gg \hat{\epsilon}$, i.e. if β is large, which in essence is the case of Smith & Li (2002), Wilson (2003)

and Wilson & Smith (2005*b*). Turbulent dominance where β is small is a practically realizable regime, however, and forms our focus, after the following section.

4. Similarity solutions

In the far field downstream, beyond any entry effects near the start of the bend, similarity solutions hold for $\tilde{\tilde{u}}, \tilde{\tilde{v}}$. The subsections below describe the respective solutions, which are further confirmation of the β-split introduced in the previous section, and are followed by numerical results.

4.1. *Solution for* $\tilde{\tilde{u}}$

With $\eta = \bar{z}/x$ and $\tilde{\tilde{u}} = \bar{f}(y) f(\eta)$, (A 1) together with (3.5) gives

$$-\eta f' = \begin{cases} 2a_2 \eta \bar{f} f'(f' + \eta f''), & \eta < \eta_J, \\ bf'', & \eta > \eta_J, \end{cases} \tag{4.1}$$

where $'$ denotes differentiation with respect to η, $b = a_2 a_1$, and $\eta_J = \bar{z}_J/x$. In the inner part, $\bar{f}(y) = K$ for some non-zero constant K, leading to $\eta f' = 0$ or $f' + \eta f'' + (2a_2 K)^{-1} = 0$. The first of these implies that the logarithmic merging with the inner tier is not possible and so the second option applies, which with $h = \eta f'$ yields the solution $h = -\eta/2a_2 K + c_5/K$ for a constant c_5. Therefore

$$f = -\frac{1}{2a_2 K}\eta + \frac{c_5}{K}\ln(\eta) + \frac{d_3}{K}, \tag{4.2}$$

for a constant d_3. The lower boundary condition requires c_5 to be unity, leaving $\tilde{\tilde{u}} = -\eta/2a_2 + \ln(\eta) + d_3$ in the inner layer.

In the outer part we have

$$\int_\eta^\infty f' \,\mathrm{d}\bar{\eta} = \frac{c_6}{K}\int_\eta^\infty \exp\big((\eta_J^2 - \bar{\eta}^2)/2b\big)\,\mathrm{d}\bar{\eta}, \tag{4.3}$$

where c_6 is an unknown constant scaled on $\exp(\eta_J^2/2b)$. (Scaling on the integrating factor ensures that numerical work concerning $\tilde{\tilde{u}}$ involves finite values.) Using the upper boundary condition $\tilde{\tilde{u}} \to 0$ as $\bar{z} \to \infty$ yields the solution:

$$\tilde{\tilde{u}} = c_6 \int_\infty^\eta \exp\big((\eta_J^2 - \bar{\eta}^2)/2b\big)\,\mathrm{d}\bar{\eta}. \tag{4.4}$$

As discussed above, the downstream streamwise behaviour is very similar to that for flow over a flat plate at zero incidence.

The remaining unknown constants c_6, d_3, η_J are determined by the three junction conditions of continuity of f, f', and the stress $\eta^2 f' = a_1$ across η_J, giving $(\eta_J, c_6, d_3) = (0.3022, 0.184, 2.14)$. Hence

$$\tilde{\tilde{u}} = \begin{cases} -\dfrac{1}{2a_2}\eta + \ln(\eta) + 2.14, & \eta < 0.3022, \\ 0.184\displaystyle\int_\infty^\eta \exp((0.3022^2 - \bar{\eta}^2)/2b)\,\mathrm{d}\bar{\eta}, & \eta > 0.3022. \end{cases} \tag{4.5}$$

Matching near the wall also yields $k_1 = \beta U_{wall}(y) + 2.14 - \ln(x)$. The effects of the core flow carried down through the layer by the $\bar{z}$-independent term βU_{wall} are felt by the inner tier through the deficit function k_1. In a similar fashion, $\beta^2 V_{wall}$ contributes to the $O(1)$ deficit function k_2, and y-dependence emerges in the inner layer.

4.2. *Solution for* $\tilde{\tilde{v}}$

The similarity form is $\tilde{\tilde{v}} = x^{\Lambda}\bar{g}(y)g(\eta)$, where Λ is zero in the straight section and unity in the bent section. Substitution into (A 4) gives:

$$x^{\Lambda-1}\bar{g}(\Lambda g - \eta g') + 2\hat{K}_2(\Lambda)f = \begin{cases} a_2 x^{\Lambda-1}\bar{g}(\eta^2 f' g')', & \eta < \eta_J, \\ b x^{\Lambda-1}\bar{g} g'', & \eta > \eta_J, \end{cases} \tag{4.6}$$

where we recall that f is known.

The general bent case, where $\Lambda \equiv 1$ and $\hat{K}_2$ is non-zero, has the following for g in the inner part,

$$\bar{g}g - a_2\bar{g}g' - a_2\eta\bar{g}g''\left(1 - \frac{1}{2a_2}\eta\right) + \hat{K}_2\left(-\frac{1}{a_2}\eta + 2\ln(\eta) + 4.28\right) = 0. \tag{4.7}$$

Separation of variables shows that $\bar{g}(y) \propto \hat{K}_2$. Without loss of generality we take the magnitude of the constant of proportionality to be 2. In the limit as $\eta \to 0+$, (4.7) is satisfied only if the separation constant is positive: $\tilde{\tilde{v}} = 2\hat{K}_2 x g(\eta)$. Although an analytical solution, based on the hypergeometric equation, to the inner part can be written down, we will concentrate instead on a more useful numerical solution described in § 4.3.

In the outer part, (4.6) leads to the solution

$$g = 0.184\frac{\bar{A}}{b}\exp\left(y_J^2/2b\right)\int_{\infty}^{y} I\,\mathrm{d}\bar{y} - 0.184\exp\left(y_J^2/2b\right)I \quad \text{where} \quad I = \int_{\infty}^{y}\exp(-\bar{y}^2/2b)\,\mathrm{d}\bar{y}, \tag{4.8}$$

with $\bar{A}$ unknown.

The y-dependence in the velocity components is thus as follows. For both $\tilde{u}, \tilde{v}$, the y-dependence arises from the matching with the core flow's y-dependence carried down across the whole layer. By contrast, for $\tilde{\tilde{u}}$ we defined $\tilde{\tilde{u}} = \bar{f}(y)f(\eta)$, but showed that $\bar{f}$ is in fact a constant: there is no y-dependence. Finally, we defined $\tilde{\tilde{v}} = x\bar{g}(y)g(\eta)$ and showed that $\bar{g} = 2\hat{K}_2$ after a similar scaling-out, with $\hat{K}_2$ giving the y-dependence.

4.3. *Numerical solutions*

The inner part, (4.7), is solved numerically. This ODE has a singularity at $\eta = 2a_2 = 0.32$ outside but neighbouring the computational range $\eta < \eta_J = 0.3022$. There are three junction conditions to satisfy: continuity of g, g' and stress. The last is satisfied automatically here once the first two hold, owing to the isotropic eddy viscosity. We start the computations at $\eta = \Delta \ll 1$ to avoid the singularity in the driving term $\ln(\eta)$ at the wall. Although the lower boundary condition on g is known because $g = 0$ there to satisfy the no-slip condition, $g'(\Delta)$ is not known, since the deficit function for g has not been determined. Our computation of g is direct, treating the initial-value problem as a boundary-value problem, with a 'known' junction value for g of zero, since it is certainly close to zero there and decays monotonically thereafter.

The distance offset from the wall Δ is fixed by comparing the computed results with the wall asymptote. Care must be taken because while the controlling behaviour of the asymptote seems to be $\eta\ln(\eta)/a_2$, this comes from the driving term f, the particular integral of the solution of the ODE; but by supposing that $g \sim \lambda\eta^m$ for some $m \geqslant 0$ and $\lambda \neq 0$ as $\eta \to 0+$, the complementary function is found to be $A + B\ln(\eta)$, for constants A and B, and hence

$$g \sim A + B\ln(\eta) + C\eta\ln(\eta) + D\eta + O(\eta^2\ln(\eta)) \quad \text{as } \eta \to 0+. \tag{4.9}$$

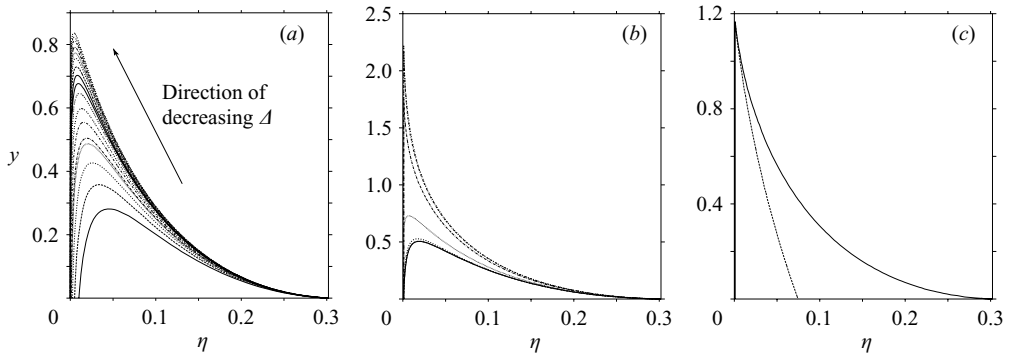

FIGURE 2. (*a*) The appearance of a numerical boundary layer. Seventeen datasets are shown with Δ ranging from 0.01 to 0.0000001. In each uniform grid, the distance between two grid points was at least an order of magnitude less than Δ. (*b*) Curves generated by successive refinements of the grid between $\Delta = 0.001$ and the second point of the standard grid of 100 000 points. Increasing the refinement increases monotonically the maximum value of g. The lowermost curve has no refinement, whilst the uppermost features an additional 1 000 000 points. (*c*) The solution parallel to the quoted near-wall asymptote, and the asymptote itself (dotted line) with $A = 1.21$.

As the inner tier is entered, $\eta \to \hat{\epsilon}^{-2} Re^{-1} \tilde{\eta}$ such that $\ln(\eta)$ becomes $-2\ln(\hat{\epsilon}) - \ln(Re) + \ln(\tilde{\eta})$. B is zero in general to satisfy the no-slip condition at the wall, and substituting (4.9) into the full equation gives $g \sim A + \eta \ln(\eta)/a_2 + (A + 0.14)\eta/a_2$ as $\eta \to 0+$, where the constant A is arbitrary. This necessitates transforming the equation, because setting $g = 0$ at the wall is false, and yet a non-zero value corresponding to A cannot be set there since it is not fixed by the equations. Furthermore, on this length scale, the solution should asymptote to a constant at the wall with the $\eta \ln(\eta)$-behaviour occurring extremely close to the wall, the constant term being cancelled by a corresponding term in the inner tier expansion.

After applying the transform $S = g/\ln(\eta)$ in the governing equation, the boundary condition at $\eta = \Delta$ becomes $S(\Delta) = 0$, with the form of S suggesting that the adjustment to this boundary condition should happen over a length scale so short as to be practically invisible, and thus the asymptote to a constant value at the wall would be apparent.

At first, only a numerical boundary layer appears as Δ decreases, with the solutions tending to a universal curve, as shown in figure 2(*a*). Although this is persuasive, the large η-range over which g adjusts is puzzling. To feed more information into the system over the crucial adjustment region, we used grid refinement between the first two computational-grid points of a standard grid with a constant spacing of grid points. The grid spacing δ was one order of magnitude less than Δ; refinement beyond this did not improve the results. Increasing the refinement with Δ fixed, generates an adjustment over a short distance and gives a variety of curves, as shown in figure 2(*b*). The level of refinement was chosen to generate a curve parallel to the asymptote $A + \eta \ln(\eta)/a_2$ near the wall, and then A was fixed such that the curve of the solution and the curve of the asymptote coincide there. This solution and the asymptote are shown in figure 2(*c*).

This result is not an artefact of the grid nor an artifice of the user because the result is grid-independent in the following way. With $\Delta = 0.001$, the solution shown in figure 2(*c*) has a standard grid of 100 000 points between Δ and η_J with a 3000-point refinement near the wall. If the grid refinement density is defined as $(N_r + N_s)N_s^{-1}$

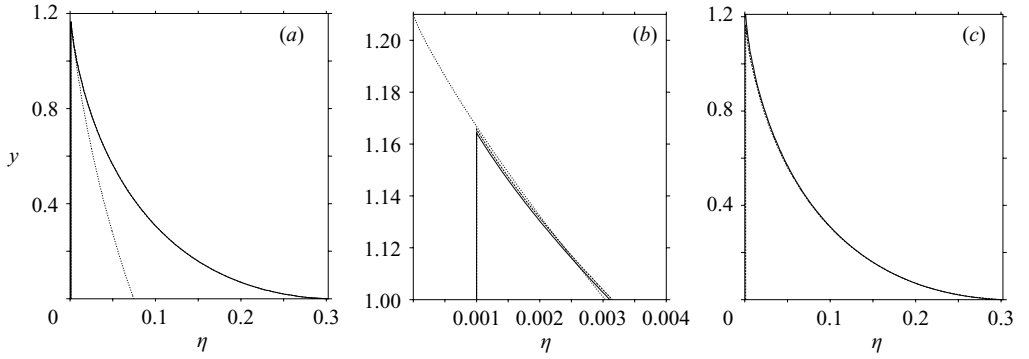

FIGURE 3. The solid line in (*a*) is in fact two lines; the solutions from both grids coincide at this scale. The dotted line is the near-wall asymptote. In the magnified view in (*b*), a small difference can be seen between the two solutions. (*c*) A comparison of the transform method results of figure 2 (dotted line) with those of a direct computation of g after setting $g(\Delta) = 1.21$.

where N_r is the number of refinement points between two standard points and N_s is the number of standard points, then this grid has a grid refinement density of 103%. A second computation with the same refinement density between points 1 and 2 of the standard grid was performed with a 500 000-point standard grid, and the two sets of results are compared in figures 3(*a*) and 3(*b*), together with the asymptote. The results compare very favourably indeed. A final assurance comes from a direct computation of g (without the transform) over a 100 000-point standard grid (with no refinement), and forcing $g(\Delta = 0.001) = 1.21$. The result is very close to that for the transform method with grid refinement, as shown in figure 3(*c*).

Flows in which, as in our results, the crossflow involves a maximum velocity very close to the surface have been observed experimentally in Zhang & Lakshminarayana (1990), a study of turbulent boundary layers over curved turbomachinery blades. Although for an external flow with wall curvature, the data for the crossflow over such a blade shows the maximum of the crossflow velocity very close indeed to the blade surface.

5. The merging turbulent wall layers

When β is small, the turbulent wall layers grow to merge and fill the pipe at a distance $O(\hat{\epsilon}^{-1})$ downstream, and so we now consider the merged (or merging) wall layers in quasi-straight two-dimensional ducts (§§ 5.1, 5.2) and three-dimensional pipes (§ 5.4) over that distance, along with experimental comparisons in §§ 5.3, 5.5. Between the entry and merged regions the dominant velocity perturbations in the core are due to the blocking effect of the growing layers. In § 6, wall frictional effects caused by the turbulent wall layer are compared with Fanno flow.

5.1. *When planar turbulent effects dominate*

Lengths are non-dimensionalized on the duct half-width here rather than the duct width, to avoid factors of 1/2 in flow development between the wall and the centreline. Now $x = \hat{\epsilon}^{-1}X$, where X is $O(1)$, and the wall-normal coordinate z is $O(1)$ (see figure 4). The slender-layer approximation clearly also holds at this stage. The full velocities

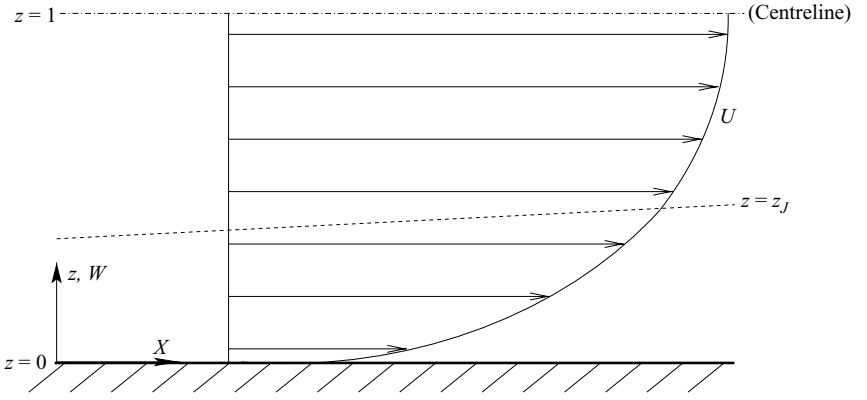

FIGURE 4. Coordinate configuration when planar turbulent effects dominate.

are now denoted by U, W, and mass conservation gives

$$\int_0^1 U_x \, \mathrm{d}z = 0, \tag{5.1}$$

since there is no normal flow at the wall or across the centreline; hence, U has a uniform leading term such that

$$U \sim 1 + \hat{\epsilon}\hat{U}(X, z), \quad W \sim \hat{\epsilon}^2 \hat{W}(X, z). \tag{5.2}$$

The continuity balance is related to the streamfunction component ψ_1 via $\psi_{1z} = \hat{U}$, $\psi_{1X} = -\hat{W}$, where ψ_1 is zero on both $z = 0, 1$ since there is a non-dimensional mass flux of 1 in each half of the duct, and

$$\int_0^1 \hat{U}(X, z) \, \mathrm{d}z = 0 \quad \text{for all } X. \tag{5.3}$$

The turbulent slender-layer x-momentum equation applies without curvature,

$$UU_x + WU_z = -p_x + \frac{1}{Re}\nabla^2 U + (BU_z)_z, \tag{5.4}$$

with $Re \gg 1$ and the Cebeci–Smith model

$$B = \begin{cases} a_2 z^2 \left[1 - \exp\left(- \dfrac{Re^{1/2}}{26} z(|(U_z)_{wall}|)^{1/2} \right)\right]^2 |U_z|, & z < z_J, \\ a_1 U_{C_L} \delta_1, & 1 > z > z_J. \end{cases} \tag{5.5}$$

Here, the effective displacement is $\delta_1 = \int_0^1 (1 - U/U_{C_L}) \, \mathrm{d}z$, where U_{C_L} is the streamwise centreline velocity. In fact, $\delta_1 \sim \hat{\epsilon}\hat{\delta}_1$ with $\hat{\delta}_1 = \hat{U}_{C_L} - \int_0^1 \hat{U} \, \mathrm{d}z = \hat{U}_{C_L}$, by (5.3), i.e. $\delta_1 \sim \hat{\epsilon}\hat{U}_{C_L}$. Since $\hat{U}_{C_L}$ appears in the outer part of (5.5), it is clear that $\hat{U}_{C_L}$ is an important parameter in the present merged two-dimensional quasi-straight regime. The pressure is $p \sim 1 + \hat{\epsilon} p_1(X) + \hat{\epsilon}^2 p_2(X, z)$ and the streamwise-momentum equation becomes

$$\hat{U}_X = -p_{1X} + \begin{cases} a_2 \left(z^2 \hat{U}_z^2\right)_z, & z < z_J, \\ \bar{a}_1 \hat{U}_{zz}, & z_J < z < 1, \end{cases} \tag{5.6}$$

where $\bar{a}_1 = a_1 \hat{U}_{C_L}$. The lower boundary condition on $\hat{U}$ remains $\hat{U} \sim 1 \times \ln(z)$ as $z \to 0+$.

By integrating (5.6) across the half-width of the duct we obtain

$$p_{1X} = -a_2 \quad \text{for all } X, \tag{5.7}$$

and as a consequence we have:

$$\hat{U}_X = a_2 + \begin{cases} a_2\left(z^2\hat{U}_z^2\right)_z, & z < z_J, \\ \bar{a}_1\hat{U}_{zz}, & z_J < z < 1. \end{cases} \tag{5.8}$$

Equation (5.8) and the corresponding boundary conditions are central to the rest of this section. We also note immediately that the result that $p_{1X} = -a_2 = -0.16$ depends only on the assumption of the mixing-length hypothesis and not on the choice of model. This can be seen by tracing the development of the Cebeci–Smith model from Prandtl's mixing-length model.

5.2. *Numerical study*

Differentiation of the inner part of (5.8) gives an equation for $\tau = \hat{U}_z$. We then set $T = (z\tau)^2$, so that the inner part of (5.8) becomes $T^{-1/2}T_X = 2a_2 z T_{zz}$, which is a nonlinear diffusion equation. By defining the junction-fitted inner coordinate $\eta = z/f$, this equation becomes

$$T_X = \frac{\eta}{f}\left(f'T_\eta + 2a_2 T^{1/2}T_{\eta\eta}\right). \tag{5.9}$$

The wall condition $\hat{U} \sim 1 \times \ln(z)$ and the junction condition of continuity of stress impose

$$T(\eta = 0) = 1, \quad T(\eta = 1) = \left(\frac{\bar{a}_1}{a_2 f}\right)^2. \tag{5.10}$$

The main equations here are therefore (5.9) and (5.10).

For the outer part of (5.8), differentiating implies a linear diffusion equation for τ. We define the junction-fitted outer coordinate $\hat{\eta} = (z-1)/(f-1)$ such that $\hat{\eta} = 0$ at the centreline and $\hat{\eta} = 1$ at the junction, so that

$$\tau_X = \frac{1}{(f-1)^2}((f-1)f'\hat{\eta}\tau_{\hat{\eta}} + \bar{a}_1\tau_{\hat{\eta}\hat{\eta}}). \tag{5.11}$$

Symmetry across the centreline, and continuity of $\hat{U}_z$ across the junction yield the requirements

$$\tau(\hat{\eta} = 0) = 0, \quad \tau(\hat{\eta} = 1) = \frac{\bar{a}_1}{a_2 f^2}. \tag{5.12}$$

Thus the main equations in the outer part are (5.11) and (5.12).

The above systems were solved numerically as follows. The governing equations are parabolic in X and we assumed that there is no reverse flow in order to use a forward-marching approach. We discretized with nominally first-order accurate backward differencing formulae for the X derivatives, and with second-order accurate central-space difference formulae for the η and $\hat{\eta}$ derivatives. The computational grids were fitted to the unknown curve $z_J = f(X)$ by the use of η, $\hat{\eta}$; then $f(X)$ was linearly optimized at each X-station. A higher-order scheme was not applied simply because the higher-order behaviour of $\hat{U}$ near the wall is unknown here, and furthermore $\hat{U}_{zz}$ can be shown to be discontinuous at $z = z_J$. Given the junction position, the inner equation (5.9) and the outer equation (5.11) together with their associated boundary and junction conditions form two closed boundary-value problems. Each is tackled

independently before comparing values across $\eta = 1 = \hat{\eta}$ to determine the junction position, as follows.

With an initial guess for f we solve (5.9) for T and (5.11) for τ, with the current guess for f diffusing through the computational domain of each boundary-value problem via the computational boundaries. The important parameter $\hat{U}_{C_L}$ is updated by

$$(\hat{U}_{C_L})_X = a_2 + \left.\frac{\bar{a}_1 \tau_{\hat{\eta}}}{f-1}\right|_{\hat{\eta}=1}. \tag{5.13}$$

The nonlinearity of (5.9) and (5.11) requires lagging of some of the variables and so iteration is used. Continuity of $\hat{U}$ across the junction defines an error

$$E = \left| \left.\frac{\bar{a}_1 \tau_{\hat{\eta}}}{f-1}\right|_{\hat{\eta}=1} - \left.\frac{a_2 T_\eta}{f}\right|_{\eta=1} \tau \right|, \tag{5.14}$$

which we minimize to optimize f. The computation is then repeated with this optimized value of f before advancing to the next X-station. This solution method had higher-order accuracy than a computed predictor–corrector approach, and we will present only the high-order accurate results. If required, $\hat{U}$ can be determined by integrating the computed values of τ and T between 1 and z since we know $\hat{U}_{C_L}$. Continuing, ψ can be found by integration either from 1 to z or from 0 to z.

The starting conditions are determined by considering (5.9), (5.11) where X is small, with an inner region $f \sim d_1 X$, $T \sim T_0(\eta)$, with the constant d_1 and the function T_0 to be determined. Then (5.9) has solution

$$2\left(T_0^{1/2} - d_2 \ln\left(T_0^{1/2} + d_2\right)\right) = -\frac{d_1}{a_2}\eta + d_3, \tag{5.15}$$

where d_2 is an unknown constant and $d_3 = 2(1 - d_2 \ln(1 + d_2))$ by (5.10). After rescaling $\bar{a}_1$ by $\bar{a}_1 = \tilde{a}_1 f$, the junction condition (5.10) yields $T_0(1) = (\tilde{a}_1/a_2)^2$. Substituting this into (5.15) yields

$$\frac{2\tilde{a}_1}{a_2} + \frac{d_1}{a_2} - 2 = d_2 \ln\left(\frac{\tilde{a}_1}{a_2} + d_2\right) - 2d_2 \ln(1 + d_2) \tag{5.16}$$

at the junction, which will later help to determine the unknown constants. Next, the junction matching condition suggests that $\tau \sim X^{-1}\hat{\tau}(\hat{\eta})$ where, after some working with $\hat{\eta} = 1 - X\hat{\hat{\eta}}$,

$$\hat{\tau} = d_5 \exp\left(\frac{-(\hat{\hat{\eta}} + d_1)^2}{2\tilde{a}_1 d_1}\right). \tag{5.17}$$

The junction condition occurs where $\hat{\hat{\eta}} = 0$, which yields

$$d_5 = \frac{\tilde{a}_1}{a_2 d_1} \exp\left(\frac{d_1}{2\tilde{a}_1}\right). \tag{5.18}$$

Next, the optimizing condition (5.14) for an exact match of U_X across the junction is

$$-d_1^2 d_5 \exp\left(\frac{-d_1}{2\tilde{a}_1}\right) = -\frac{d_1}{a_2}(\tilde{a}_1 + d_2 a_2). \tag{5.19}$$

With d_5 known from (5.18) we have d_2 zero, and hence $d_3 = 2$. Finally, (5.16) now gives $d_1 = 2(a_2 - \tilde{a}_1)$. All the constants are therefore determined, and $f \sim d_1 X$, $\hat{U}_{C_L} \sim a_2 X$ are the local asymptotes.

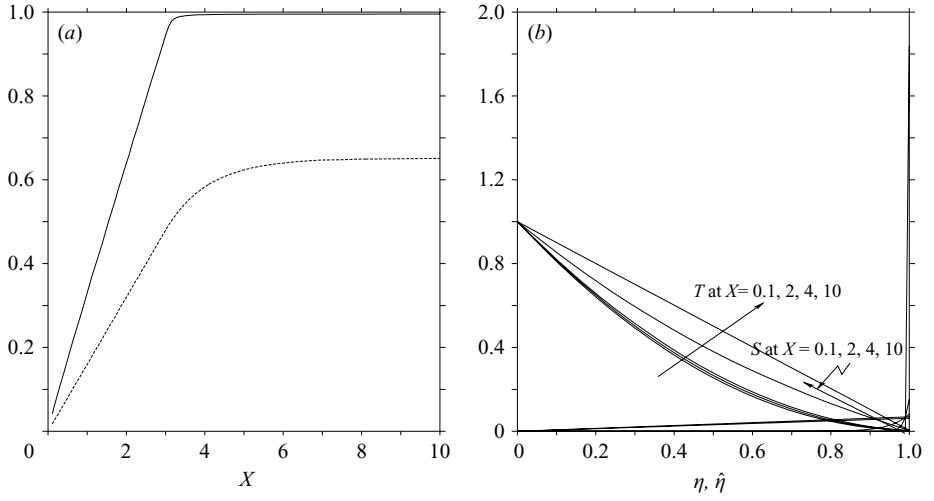

FIGURE 5. (*a*) Plot of f (solid) and $\hat{U}_{C_L}$ against X. (*b*) The development of T and S with X.

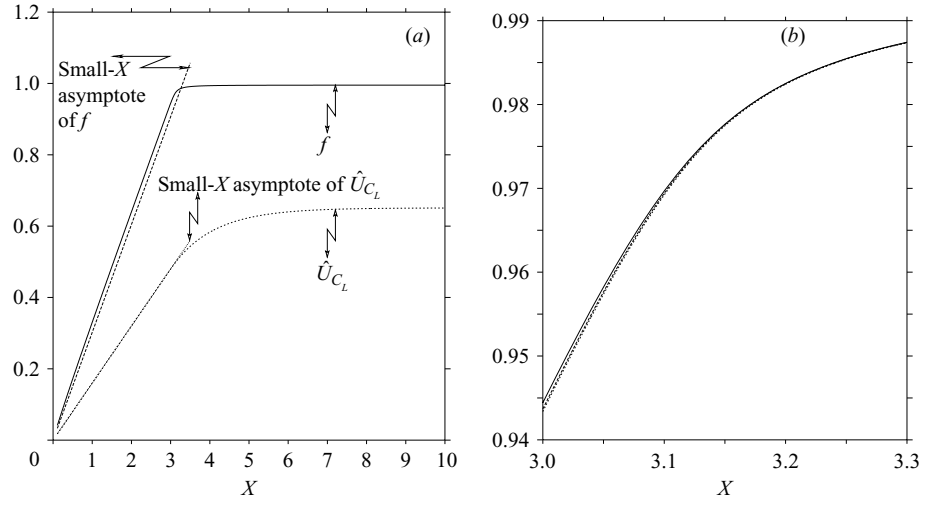

FIGURE 6. (*a*) f, $\hat{U}_{C_L}$, and their small-X asymptotes. (*b*) Close-up of the sudden bending of f, showing results over three grids with step $dX = 0.01, 0.001, 0.0001$ and suitable refinements of the η and $\hat{\eta}$ step sizes.

The numerical scheme was run over a variety of grids, and grid-convergence of the results was demonstrated. A typical grid had 101 points in both the η-layer and the $\hat{\eta}$-layer, an X-step size of 0.01, and was tested to an accuracy of 10^{-10}. We determined for each grid a small value of X from which to start the computation and for which the results were stable over small modifications to this value. In the case of the above grid, the computation was started from $X = 0.1$. The results of this computation are shown in figure 5.

The developments of $f, \hat{U}_{C_L}$ are virtually linear until around $X = 3.5$, where a sudden bending occurs over a short distance and a far-downstream asymptote appears to be reached relatively quickly. Figure 6(*a*) shows that the linear growths which occur for $O(1)$ values of X are very close to the small-X asymptotes of $f, \hat{U}_{C_L}$, and we

investigate the sudden bending away from the small-X asymptotes in Appendix B. Figure 6(b) shows that the location of the bending is stable over a variety of grids. What is more, the values of $f(X=10)$ were stable to three decimal places over all grids which showed convergence, and the values of $\hat{U}_{C_L}(X=10)$ agreed to two decimal places. These far-downstream asymptotes are

$$f(10)=0.995, \quad \hat{U}_{C_L}(10)=0.65. \tag{5.20}$$

The apparent attainment of constant values of f and $\hat{U}_{C_L}$ – fully developed flow – for large values of X suggests examining (5.8) there. Its inner part becomes $T_{zz}=0$ if X-derivatives are negligible far downstream and so

$$T=\left(\left(\frac{\bar{a}_1}{fa_2}\right)^2-1\right)\frac{z}{f}+1 \quad \text{as} \quad X\to\infty. \tag{5.21}$$

The outer part similarly becomes $\tau_{zz}=0$ and (5.12) then yields

$$\tau=\frac{\bar{a}_1(z-1)}{a_2f^2(f-1)}. \tag{5.22}$$

Continuity of U_X across the junction $z=f$ requires $\bar{a}_1\tau_z=a_2T_z$ at $z=f$, giving

$$a_2^2(f^3-f^2)+\bar{a}_1^2=0. \tag{5.23}$$

Since $\bar{a}_1=a_1\hat{U}_{C_L}$, (5.23) gives a value for f far downstream only when $\hat{U}_{C_L}$ is already known there. Thus, not only is $\hat{U}_{C_L}$ an important parameter in the flow development here, but it is also an important net effect, since it influences the downstream asymptote. It would seem that in order to determine $\hat{U}_{C_L}$ at a far-downstream position, a full computation in the development region leading up to the fully developed region must be done (as for example in our results). This is certainly different from the laminar case where a knowledge of the pressure difference alone between the start and the fully developed region provides the centreline velocity. On the other hand, the linear growth in line with the small-X asymptote, coupled with the sudden bending and attainment of the large-X asymptote described above, indicate a useful predictive tool for $\hat{U}_{C_L}$, f which we describe in Appendix B, wherein we also demonstrate analytically that the sudden bending of f is smoothed on a short length scale.

Finally here, if we substitute the computed large-X values of $\hat{U}_{C_L}(10)$ given in (5.20) into (5.23) we obtain three values for f: $0.995, 0.071, -0.066$. Only the first of these is physically realistic, and is equal to the computed large-X value of f given in (5.20), demonstrating a consistency between the current analysis and the numerical results.

5.3. *Comparisons with experiments*

In figure 7, we compare the pressure prediction (5.7) (which leads to the governing equation whose numerical solution is shown in figure 5) with the experimental data of Laufer (1949) for the two Reynolds numbers considered in that paper. It is clear that the prediction gives values which agree closely with the empirical data.

Figure 8 compares the total centreline velocity u_{C_L} derived from the numerical results with three data sets: Nakao (1986) with measured $Re=1.7\times10^5$; Chinni, Sahai & Munukutla (1996) with measured $Re=9\times10^4$; Melling & Whitelaw (1976) with measured $Re=2.07\times10^4$. The numerical results capture the nature (or much of it) and location (to varying degrees of agreement up to around 95%) of the bending, but the value of u_{C_L} is correct only to within around 85%. However, since only the first term in the expansion of u is considered, we expect higher-order terms to correct

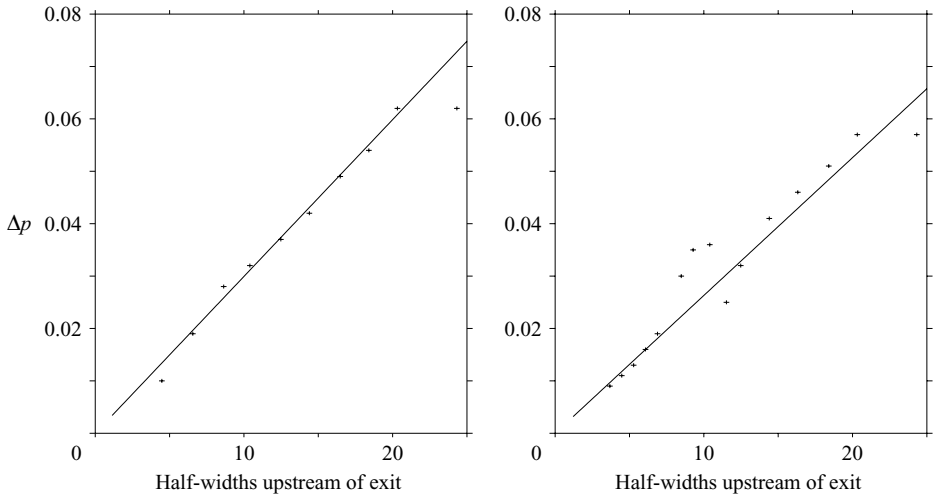

FIGURE 7. Comparison between (5.7) (line) and Laufer (1949) (*a*) at $Re = 30\,800$ and (*b*) at $Re = 61\,600$. Δp is the pressure difference from the exit of the pipe. (The half-widths here are measured from zero at the exit and increase upstream.)

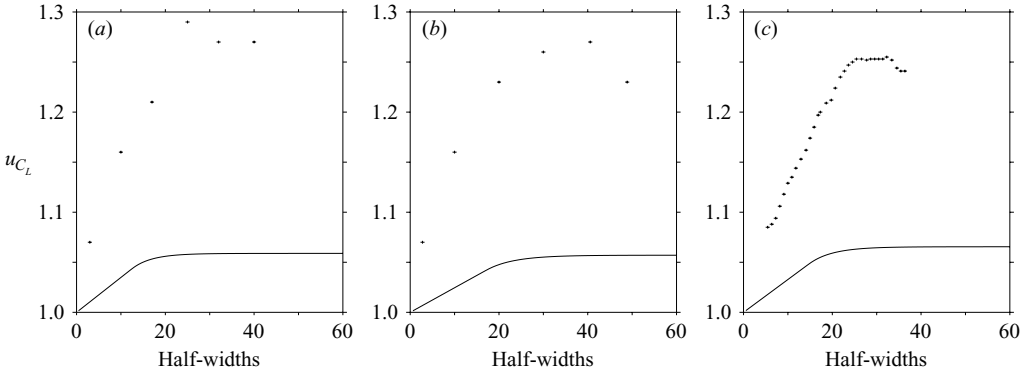

FIGURE 8. Comparisons between numerical results and (*a*) Nakao (1986), (*b*) Chinni *et al.* (1996) and (*c*) Melling & Whitelaw (1976). (Half-widths are as in figure 7.)

the value, analagously to Neish & Smith (1988, pp. 32–33). Note that in this context, the pressure predictions are very close indeed to the experimental data. Indeed the experimental data of Barbin & Jones (1963) for turbulent inlet flow in a smooth pipe showed that the pressure gradient was established within 15 pipe diameters downstream, whereas the centreline velocity was not yet established after 40.

5.4. *When turbulent effects dominate in three dimensions*

The configuration is shown in figure 9. Here, $\hat{u}_2$ remains zero in this quasi-straight case, secondary-flow-generating sharp corners are absent in an axisymmetric pipe, and we need only solve for U in the X-direction and W in the wall-normal (radial) direction.

We base our study on the full dimensional general axisymmetric equations given in Cebeci & Smith (1974, p. 259), our non-dimensionalizations being those of § 5.1, with the slender-layer approximation still applying far downstream in the merged region. We again use the Cebeci–Smith model, with the analysis holding for any two-tiered

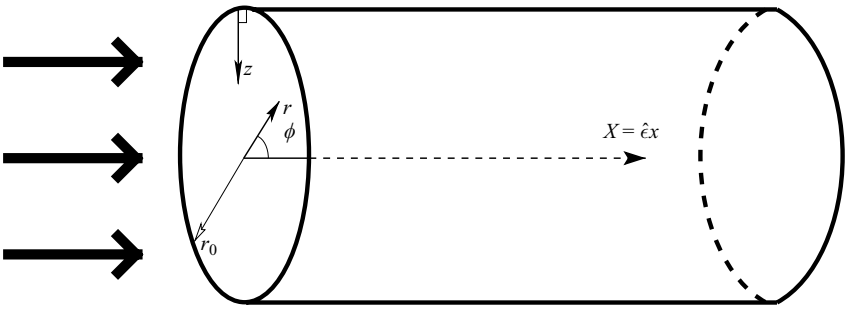

FIGURE 9. Coordinate configuration for the three-dimensional axisymmetric pipe. The boundary layer is not shown. The pipe is considerably longer than indicated here.

algebraic mixing-length model. The non-dimensional governing equations are thus:

$$((1-z)U)_x + ((1-z)W)_z = 0, \tag{5.24a}$$

$$UU_x + WU_z = -p_x - \frac{BU_z}{(1-z)} + (BU_z)_z, \tag{5.24b}$$

where, for large Re, the non-dimensional eddy viscosity is:

$$B = \begin{cases} a_2(1-z)\ln^2(1-z)U_z, & z < z_J, \\ a_1 \displaystyle\int_0^1 \left(1 - \frac{U}{U_{C_L}}\right)(1-z)\,\mathrm{d}z, & z_J < z < 1. \end{cases} \tag{5.25}$$

The curvilinear coordinate system introduces an extra factor $(1-z)$ in the continuity equation and there are now two terms in the eddy viscosity B in the x-momentum equation, while the form of B in the inner region now contains a log term.

Here, $U \sim 1 + \hat{\epsilon}\hat{U}$; $W \sim \hat{\epsilon}^2\hat{W}$; $p \sim 1 + \hat{\epsilon}p_1(X) + \hat{\epsilon}^2 p_2(X, z)$ and the quasi-displacement becomes

$$\delta_1 \sim \hat{\epsilon}\hat{\delta}_1 = \hat{\epsilon}\int_0^1 (\hat{U}_{C_L} - \hat{U})(1-z)\,\mathrm{d}z. \tag{5.26}$$

Consequently, examining (5.24*a*, *b*), (5.25) gives:

$$((1-z)\hat{U})_X + ((1-z)\hat{W})_z = 0, \tag{5.27a}$$

$$\hat{U}_X = -p_{1X} + \frac{1}{(1-z)}((1-z)\hat{B}\hat{U}_z)_z, \tag{5.27b}$$

where

$$\hat{B} = \begin{cases} a_2(1-z)\ln^2(1-z)\hat{U}_z, & z < z_J, \\ a_1\hat{\delta}_1, & z_J < z < 1. \end{cases} \tag{5.27c}$$

The boundary conditions as $z \to 0+$ are:

$$\hat{U} \sim 1 \times \ln(z), \quad \hat{W} = 0. \tag{5.28}$$

Equations (5.27*a*, *b*) can be solved independently for $\hat{U}, \hat{W}$.

In Appendix C, we use the smallness of a_1 to show that the centreline velocity increases linearly with X over an $O(1)$ section in the X-direction, and that far downstream the junction position $z_J = f(X)$ is constant and lies very near the pipe centreline.

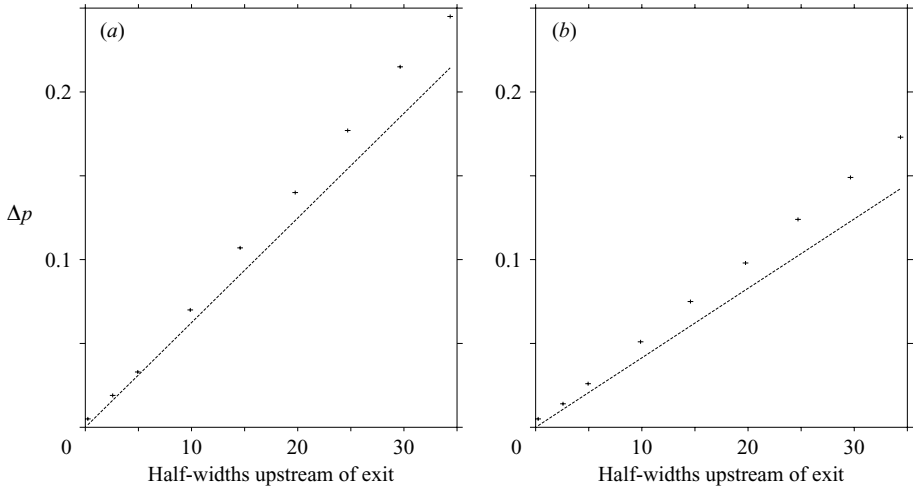

FIGURE 10. Comparison between (5.31) (line) and Laufer (1952) (*a*) at $Re = 25\,000$ and (*b*) at $Re = 250\,000$. Δp is the pressure difference from the exit of the pipe. (Half-widths are as in figures 7 and 8, measured from zero at the exit and increasing upstream.)

5.5. *Further comparisons with experiments*

Integration of (5.27*a*) gives:

$$\int_0^1 \hat{U}(1-z)\,\mathrm{d}z \equiv 0 \tag{5.29}$$

for all X (since $\hat{U}$ is zero at $X \to 0+$). Thus

$$\hat{\delta}_1 = \tfrac{1}{2}\hat{U}_{C_L}. \tag{5.30}$$

This prediction is 1/4 that in the two-dimensional duct, indicating a considerable difference between the two-dimensional and three-dimensional axisymmetric cases.

Integrating (5.27*b*) over the cross-section, using (5.29), symmetry at the centreline, and the wall boundary condition (5.28) on $\hat{U}$ gives

$$p_{1X} = -2a_2, \tag{5.31}$$

which predicts a pressure gradient twice as great as in the two-dimensional case.

The prediction (5.31) can be compared with the experimental data of Laufer (1952) for $Re = 2.5 \times 10^4$ and $Re = 2.5 \times 10^5$ as we have defined Re, in a plot against distance in half-widths measured from zero at the exit and increasing upstream, as shown in figure 10. The prediction (5.31) compares very well with the experimental values particularly near the exit of the pipe where perhaps the flow is more fully developed.

6. Fanno flow effects

These concern mean values near the start of the quasi-straight pipe where the wall layer is not fully merged, (5.27*b*, *c*) apply, but (5.29) no longer holds. With the mean

value for the variable $\hat{U}(X, z)$ being

$$\bar{U}(X) = \frac{\displaystyle\int_0^{2\pi}\int_0^1 \hat{U}(1-z)\,\mathrm{d}z\,\mathrm{d}\phi}{\displaystyle\int_0^{2\pi}\int_0^1 1\times(1-z)\,\mathrm{d}z\,\mathrm{d}\phi} = \frac{\displaystyle\int_0^{2\pi}\int_0^1 \hat{U}(1-z)\,\mathrm{d}z\,\mathrm{d}\phi}{\pi}, \tag{6.1}$$

(5.27*b*, *c*), (5.28) yield

$$(\bar{U} + p_1)_X = 2a_2\big[-(1-z)^2\ln^2(1-z)\hat{U}_z^2\big]|_{z\to 0+} = -2a_2. \tag{6.2}$$

On the other hand, the Fanno flow model in a circular pipe (see e.g. Knight 1998) has $\rho_D u_D u_{Dx_D} + p_{Dx_D} = -2F_D u_D^2/D_D$, where the subscript $_D$ represents dimensional quantities, F_D is the wall friction factor, and D_D is the diameter of the circular pipe. In the present incompressible case, we take $F_D = \rho_D F$ and thus Fanno flow is governed by $uu_x + p_x = -(2Fu^2)/D$, which in the merged case becomes to leading order

$$\hat{U}_X + p_{1X} = -\frac{2F}{\hat{\epsilon}^2\pi}. \tag{6.3}$$

A typical mean friction factor is $F = 0.005$ (Knight 1998; Ockendon, Ockendon & Falle 2001). For (6.2), (6.3) to agree here thus requires $F = 0.16\pi(\ln(Re))^{-2}$, corresponding to a Reynolds number of approximately $Re \approx 2.26\times 10^4$, which is certainly within the range of Re considered in this paper. This therefore shows that the wall frictional effects in a pipe can be modelled in a partial manner by the mean influences of the growth of the turbulent wall layer described by (any) two-tier mixing-length model.

7. Further comments

An immediate point is that the parameter $\hat{U}_{C_L}$ (the centreline velocity contribution) has 'memory', in that it is coupled with the total flow development and cannot simply be predicted, even in fully developed motion, from a knowledge of the pressure gradient in the pipe. At first sight, the strong dependence of the flow on $\hat{U}_{C_L}$ coupled with the memory of $\hat{U}_{C_L}$ suggests that, in most flow situations, a substantial calculation must be performed in order to determine the far-downstream fully developed form. On the other hand, a potentially powerful predictive tool is suggested by the development of f (junction position) and $\hat{U}_{C_L}$, as supported by the Appendices, in which in outline $f, \hat{U}_{C_L}$ first grow linearly, exactly in line with their entry-region asymptotes, and then both curves bend suddenly (where the junction position closely approaches the centreline) and attain their far-downstream uniform values within a very short streamwise distance. This behaviour is apparent from the numerical results and is consistent with asymptotic study.

More generally, this paper has been concerned with the growth and development of the turbulent flow in a slender bent pipe of simple cross-section. The work holds for any two-tier mixing-length model of the eddy viscosity. The velocities split into a core-flow influence and a fully turbulent part which in the streamwise direction behaves as in turbulent flow over a flat plate. There is in general a non-zero cross-flow. We derived solutions for both the fully turbulent streamwise and the cross-flow velocities, the former having no dependence on the coordinate which runs around the pipe, whereas the cross-flow velocity does. The latter asymptotes to a constant value on approach to the wall before reaching a maximum just outside the laminar

sublayer (in line with experiments) and tending to zero at the wall. The three distinct downstream regimes in the bent pipe depend on the relative magnitudes of the swirl in the core flow and the turbulent fluctuations: the quasi-straight merged turbulent flow; the interaction regime; and the regime in which the turbulent wall layer stays thin.

The quasi-straight situation has been studied here in some detail. In the two-dimensional case, the displacement is equal to the leading-order variation in the streamwise centreline velocity and the pressure grows in proportion to the distance downstream. Computational work shows linear growth in both the junction position and the centreline velocity, followed by a sudden bending to the far-downstream asymptotes. Analysis (Appendix B) suggests that the sudden bending is smoothed over a short length scale and possibly connects with a pseudowake flow downstream. Next, the quasi-straight three-dimensional axisymmetric case was considered with predictions for the linear growth of the quasi-displacement and pressure. Analysis again suggests that the junction position increases linearly until close to the centreline before suddenly becoming constant. Predictions and numerical results were compared with experiments and empirical data, providing generally favourable agreement. Further, the effects of the turbulent wall layer described by a two-tier mixing-length model agree with Fanno flow effects in the pipe.

Extensions of the work include finding the location and cause of transition to turbulence, a study of the behaviour of the inner layer, and influence of sharp corners in the cross-section. An investigation of the behaviour of the higher-order variations of the wall-layer velocities is expected to make the pressure and centreline velocity predictions correspond more closely with empirical data. It would also be useful to perform a complete study of the downstream core–turbulent boundary-layer interaction region if the turbulent fluctuations and the core swirl are comparable in size. Moreover, a study of the proposed (Appendix B) pseudowake structure far downstream of the bending region of the two-dimensional merged case would be of interest, as would a numerical scheme to solve the three-dimensional axisymmetric merged or merging case and the extension to general cross-sections. Results could again be tested against empirical data and help to validate the predictions of the small-a_1 analysis.

This work resulted from close contacts with Sortex Ltd of London. We thank Dr Sarah Bee, Dr Mark Honeywood, and Mr Adric Marsh of Sortex Ltd for many related discussions and EPSRC and Sortex Ltd for support (P.L.W.). We also thank the referees for their helpful comments.

Appendix A. The detailed mechanics of (3.2*a*, *b*)

The $O(1)$ balance of (2.8) governing the fully turbulent term $\tilde{\tilde{u}}$ is:

$$\frac{\partial \tilde{\tilde{u}}}{\partial x} = \begin{cases} a_2 \dfrac{\partial}{\partial \bar{z}} \left(\left(\bar{z} \dfrac{\partial \tilde{\tilde{u}}}{\partial \bar{z}} \right)^2 \right), & \bar{z} < \bar{z}_J, \\ a_1 \hat{\delta}_1 \dfrac{\partial^2 \tilde{\tilde{u}}}{\partial \bar{z}^2}, & \bar{z} > \bar{z}_J. \end{cases} \tag{A 1}$$

Equation (A 1) also implies that $\tilde{\tilde{u}}$ is slowed by the stress at the wall. In reality, the stress will vary owing to curvature.

To establish (3.2*a*), we let $\tilde{u} = \tilde{u}_e + \tilde{u}_b$, where clearly $\partial\tilde{u}_e/\partial\bar{z} \equiv 0$ by definition, $\partial\tilde{u}_e/\partial x \equiv 0$ by the matching with the core flow, and $\tilde{u}_b \to 0$ as $\bar{z} \to \infty$. This form is consistent with the claim that $\tilde{u}$ is part of an exact solution for $\hat{u}$. With this, the $O(\beta)$ balance of (2.8) is:

$$\frac{\partial\tilde{u}_b}{\partial x} = \begin{cases} a_2 \dfrac{\partial}{\partial\bar{z}}\left(2\bar{z}^2 \dfrac{\partial\tilde{u}_b}{\partial\bar{z}} \dfrac{\partial\tilde{\tilde{u}}}{\partial\bar{z}}\right), & \bar{z} < \bar{z}_J, \\ a_1\hat{\delta}_1 \dfrac{\partial^2\tilde{u}_b}{\partial\bar{z}^2}, & \bar{z} > \bar{z}_J, \end{cases} \tag{A 2}$$

while the $O(\beta^2)$ balance is:

$$0 = \begin{cases} a_2 \dfrac{\partial}{\partial\bar{z}}\left(\left(\bar{z}\dfrac{\partial\tilde{u}_b}{\partial\bar{z}}\right)^2\right), & \bar{z} < \bar{z}_J, \\ 0, & \bar{z} > \bar{z}_J. \end{cases} \tag{A 3}$$

Note that β still does not appear explicitly in the equations.

The inner part of (A 3) has the solution $\tilde{u}_b = c_1\ln(\bar{z})$ for some function $c_1(x, y)$, for all $\bar{z}$ in the inner layer. As $\bar{z} \to 0+$, we enter the lower tier when $\bar{z} \to Re^{-1}\hat{\epsilon}^{-2}\tilde{z}$ (see e.g. Neish & Smith 1988, p. 23), and the above solution suggests $\tilde{u}_b \sim -c_1\ln(Re) - 2c_1\ln(\hat{\epsilon}) + c_1\ln(\tilde{z})$. This means that $u \sim 1 + \epsilon\tilde{u}_e - c_1\beta - 2c_1\epsilon\ln(\hat{\epsilon}) + \epsilon c_1\ln(\tilde{z})$ as we enter the inner tier. For the solutions (3.2*a*, *b*) to work for all orders of β as $z \to 0+$, we must take $c_1 \equiv 0$, giving $\tilde{u}_b \equiv 0$ in the inner layer. This satisfies trivially the outer part of (A 2), and also all the boundary conditions, including matching across the junction with the zero form in the inner part. This establishes (3.2*a*, *b*). In § 3.3, we show that $\tilde{\tilde{u}} \sim \ln(\bar{z}) - \beta U_{wall}(x, y)$ as $\bar{z} \to 0+$, where U_{wall} is the streamwise core flow at the wall. This, together with (3.2*a*, *b*), gives $u \sim 1 - \hat{\epsilon}\ln(Re) - 2\hat{\epsilon}\ln(\hat{\epsilon}) + \hat{\epsilon}\ln(\tilde{z}) - \epsilon U_{wall} + \epsilon U_{wall}$, with the first two and the last two terms cancelling, as required to satisfy the no-slip condition.

Turning to the y-momentum equations, (2.9), we make the substitutions (3.1*a*, *b*), and then the $O(\beta)$ balance involves the fully turbulent $\tilde{\tilde{v}}$:

$$\frac{\partial\tilde{\tilde{v}}}{\partial x} + 2\hat{K}_2\tilde{\tilde{u}} = \begin{cases} a_2 \dfrac{\partial}{\partial\bar{z}}\left(\bar{z}^2 \dfrac{\partial\tilde{\tilde{u}}}{\partial\bar{z}} \dfrac{\partial\tilde{\tilde{v}}}{\partial\bar{z}}\right), & \bar{z} < \bar{z}_J, \\ a_1\hat{\delta}_1 \dfrac{\partial^2\tilde{\tilde{v}}}{\partial\bar{z}^2}, & \bar{z} > \bar{z}_J. \end{cases} \tag{A 4}$$

To establish (3.2*b*), we assume that $\tilde{v} = \tilde{v}_e + \tilde{v}_b$, where $\partial\tilde{v}_e/\partial\bar{z} \equiv 0$ by definition, and $\tilde{v}_b \to 0$ as $\bar{z} \to \infty$. The assumption supposes that $\tilde{v}_b$ is not a constant, which we now show leads to a contradiction. The $O(\beta^2)$ balance of (2.9) is

$$\frac{\partial\tilde{v}_b}{\partial x} = \begin{cases} a_2 \dfrac{\partial}{\partial\bar{z}}\left(\bar{z}^2 \dfrac{\partial\tilde{\tilde{u}}}{\partial\bar{z}} \dfrac{\partial\tilde{v}_b}{\partial\bar{z}}\right), & \bar{z} < \bar{z}_J, \\ a_1\hat{\delta}_1 \dfrac{\partial^2\tilde{v}_b}{\partial\bar{z}^2}, & \bar{z} > \bar{z}_J. \end{cases} \tag{A 5}$$

Importantly, β no longer appears explicitly in (A 4), (A 5). Both equations are satisfied at the edge of the layer where all stresses are zero.

Equation (A 5) suggests that $\tilde{v}_b \sim c_2\ln(\bar{z})$ as $\bar{z} \to 0+$, for non-zero c_2. This leading-order behaviour near the wall implies that $v \sim \epsilon^2\tilde{v}_e + \epsilon^2 c_2\ln(\bar{z}) + \epsilon\hat{\epsilon}\tilde{\tilde{v}}$, but then $v \to \epsilon^2 c_2\ln(\bar{z})$ as $\bar{z} \to 0+$, contradicting the no-slip condition $v \equiv 0$ on $\bar{z} = 0$. Therefore,

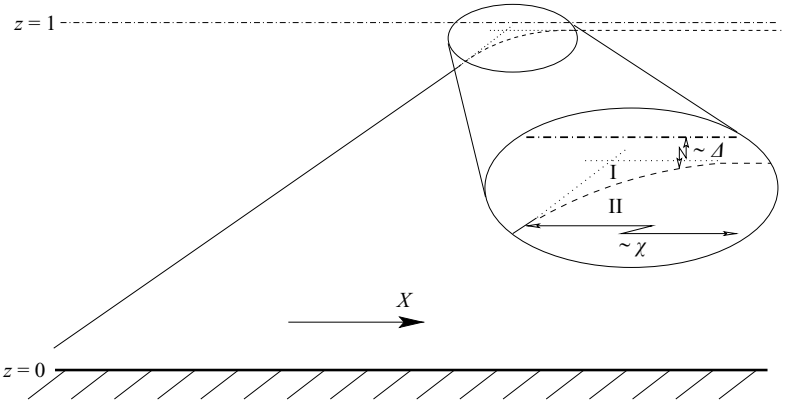

FIGURE 11. Length scales and regions of the small-$\bar{a}_1$ analysis.

$\tilde{v}_b \equiv 0$, as although any constant satisfies (A 5), only $\tilde{v}_b \equiv 0$ satisfies also the boundary condition as $\bar{z} \to \infty$. Hence, $\tilde{v} \equiv \tilde{v}_e$ exactly. We show in § 3.3 that $\tilde{\tilde{v}} \sim 2a_2^{-1}\hat{K}_2\bar{z}\ln(\bar{z}) - \beta\tilde{v}$ as $\bar{z} \to 0+$, such that $v \sim \epsilon^2\tilde{v} + \epsilon\hat{\epsilon}2a_2^{-1}\hat{K}_2\bar{z}\ln(\bar{z}) - \epsilon^2\tilde{v}$, with the first and last terms cancelling in order that v satisfies the no-slip condition.

Appendix B. Small-$\bar{a}_1$ analysis when planar turbulent effects dominate

To confirm that the sudden bending of f close to the centreline is smooth on a short length scale, we neglect the outer part of the turbulent model based on the small size of $a_1 = 0.0168$. This approximation corresponds to a rational analysis for $\bar{a}_1 = a_1\hat{U}_{C_L}$ tending to zero (Neish & Smith 1988). The major feature when $\bar{a}_1$ is small is that the two linear sections of f – the first when f increases in line with its small-X asymptote and the second when f is apparently constant – describe the majority of the solution.

Here, $X \sim X_0 + \chi\tilde{X}$, $f \sim 1 - \Delta\tilde{f}(\tilde{X})$, where X_0 is constant, and $\bar{a}_1 = \delta\hat{U}_{C_L}$ for $\delta \ll 1$, where $\hat{U}_{C_L}$ is considered an $O(1)$ constant since $\hat{U}_{C_L} = a_2X_0 + O(\chi)$. In region I of (5.8) (figure 11), τ^{I} denotes τ while τ^{II} denotes τ in region II. Since $z \sim 1$ in region II, $\tau^{\mathrm{II}} \sim \chi^{-1}$, and (5.12) gives $\tau^{\mathrm{I}} \sim \delta$. Additionally, $z = 1 - \Delta\tilde{z}$ in region I and so $\chi\delta \sim \Delta^2$. Finally, $\mathrm{d}f/\mathrm{d}X \sim 1$ in the bending region in order to match with the incoming $O(1)$ slope since $f = 2a_2X_0 + O(\delta)$ there because the small-X asymptote is $f \sim 2(a_2 - \tilde{a}_1)X$ from § 5.2. Thus, $\delta \sim \Delta \sim \chi$, which fixes the local scalings.

With $\tau^{\mathrm{I}} \sim \delta\tau^{(1)}$, the diffusion equation

$$\tau^{(1)}_{\tilde{X}} = \hat{U}_{C_L}\tau^{(1)}_{\tilde{z}\tilde{z}} \tag{B 1}$$

is subject to the conditions

$$\tau^{(1)} = 0 \text{ at } \tilde{z} = 0, \quad \tau^{(1)} = \frac{\hat{U}_{C_L}}{a_2} \text{ at } \tilde{z} = \tilde{f}(\tilde{X}), \tag{B 2}$$

requiring the junction contribution $\tilde{f}(\tilde{X})$, as discussed later. To match τ across the junction and with the incoming flow, we take

$$\tau^{\mathrm{II}} = \tau_0(z) + \delta\tau(\tilde{X}, z) + \cdots, \tag{B 3}$$

with the profile $\tau_0(z)$ known, giving

$$\tau_{1\tilde{X}} = a_2\left(z^2\tau_0^2\right)_{zz} \tag{B 4}$$

when $z \sim 1$, subject to the conditions

$$\tau_0(z) = 0 \text{ at } z = f, \quad \tau = \frac{\hat{U}_{C_L}}{a_2} \text{ at } z = f, \tag{B 5}$$

consistent with neglecting the outer part of the model. Integrating (B 4) yields

$$\tau = a_2 \tilde{X}((z\tau_0)^2)_{zz} + \frac{\hat{U}_{C_L}}{a_2}. \tag{B 6}$$

Close to the junction, where $z = 1 - \Delta\tilde{z}$, $\tau^{\mathrm{II}} \sim \delta\tau^{(2)}$ with the inner part of (5.8) becoming

$$\tau^{(2)}_{\tilde{X}} = a_2\big(\tau^{(2)2}\big)_{\tilde{z}\tilde{z}}, \tag{B 7}$$

a nonlinear diffusion problem for $\tau^{(2)}$ discussed later. The local-bending problem (B 7) has not been solved, but it allows matching upstream at large negative $\tilde{X}$ with the incident straight-f form which holds ahead of the bending region, and its downstream properties are now described.

Anticipating an $\tilde{X}$-invariant f_∞ downstream yields

$$\tau^{(1)} = \lambda_1\tilde{z} + \lambda_2 \quad \text{as} \quad \tilde{X} \to \infty \tag{B 8}$$

from (B 1), with $\lambda_2 = 0$ from (B 2) and $\lambda_1 = \hat{U}_{C_L}/(a_2\tilde{f}_\infty)$ from (B 2). Supposing for now that relatively far downstream there is no streamwise flow development to influence the junction, (B 7) in the limit $\tilde{X} \to \infty$ suggests

$$\tau^{(2)} = (\mu_1\tilde{z} + \mu_2)^{1/2}, \tag{B 9}$$

with μ_1, μ_2 unknown constants. Continuity of τ therefore requires

$$\left(\frac{\hat{U}_{C_L}}{a_2}\right)^2 = \mu_1\tilde{f}_\infty + \mu_2, \tag{B 10}$$

while continuity of $\hat{U}_X$ requires $\hat{U}_{C_L}\tau^{(1)}_{\tilde{z}} = a_2(\tau^{(2)2})_{\tilde{z}}$ at $\tilde{z} = \tilde{f}_\infty$. Furthermore, (B 8), (B 2), (B 9) give $\mu_1 = \hat{U}^2_{C_L}/(a_2^2\tilde{f}_\infty)$ and therefore $\mu_2 = 0$. In summary:

$$\tau^{(1)} \sim \frac{\hat{U}_{C_L}}{a_2\tilde{f}_\infty}\tilde{z}, \quad \tau^{(2)} \sim \frac{\hat{U}_{C_L}}{a_2\tilde{f}^{1/2}_\infty}\tilde{z}^{1/2}, \tag{B 11a,b}$$

as $\tilde{X} \to \infty$. Since the predictions (B 11a,b) were obtained by considering only the leading-order correction term, the simplifying assumption of this Appendix leads to a useful indicative tool with $\hat{U}_{C_L}$ constant.

Briefly returning to (B 7), the condition on $\tau^{(2)}$ as $\tilde{z} \to \infty$ required to match with τ in (B 3)–(B 6) raises some questions. If $\tau^{(2)} \sim c\tilde{z}$ as $\tilde{z} \to \infty$ for non-zero constant c, then (B 3) requires $\tau^{\mathrm{II}} \sim f_1(z) + \delta f_2(\tilde{X}, z)$ such that $f_1(z) \sim \delta c\tilde{z}$ as z approaches the junction. This suggests setting $f_1(z) = c(1-z)$ such that $\tau^{\mathrm{II}} \sim c(1-z) + \delta f_2(\tilde{X}, z)$, where the first term on the right-hand side matches with τ_0 and the second with τ. However, the incoming flow has $\tau = -(2a_2)^{-1} + z^{-1}$ from (4.5), which suggests that $T = (1 - z/2a_2)^2$. With the scale change, $T_0 \sim (1-z)^2$ near the junction seems to imply that $c = 0$ in the above, indicating a term in $\tilde{z}^{1/2}$ becoming important, making the downstream region very much like the wake flow in Neish & Smith (1988). The schematic configuration of the regions is represented in figure 12. The pseudowake flow for large $\tilde{X}$ feels the inflow determined by solving the nonlinear problem for $\tau^{(2)}$ and a continued development of the interface between regions I and III may invalidate the results for

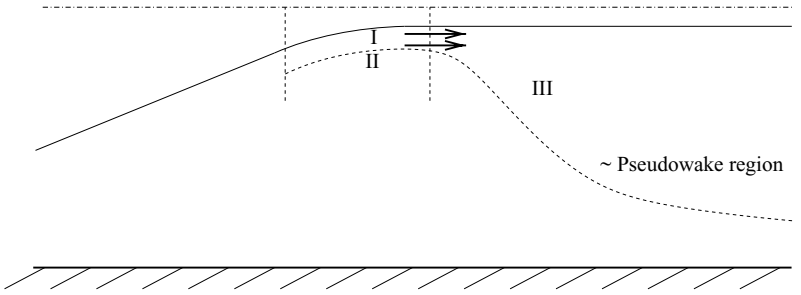

FIGURE 12. Regions of the flow field.

large $\tilde{X}$ obtained above. As the thickness of the pseudowake region increases as $\tilde{X}$, the region gradually feels the influence of the lower wall.

Finally, continuity of $\hat{U}_X$ across $z = f$ yields:

$$\hat{U}_{C_L}\tau_{\tilde{z}}^{(1)}\big|_{\tilde{z}=\tilde{f}} = 2a_2\tau^{(2)}\tau_{\tilde{z}}^{(2)}\big|_{\tilde{z}=\tilde{f}}. \tag{B 12}$$

Once the nonlinear (B 7) has been solved for $\tau^{(2)}$, (B 12) gives $\tilde{f}$ precisely and hence the linear problem for $\tau^{(1)}$, (B 8), can be solved.

Appendix C. Small-a_1 analysis when turbulent effects dominate in three dimensions

As in Appendix B, we use the smallness of a_1 to neglect the outer part of the model, giving

$$\hat{U}_X = a_2\left(2 + \frac{1}{(1-z)}\left((1-z)^2\ln^2(1-z)\hat{U}_z^2\right)_z\right) \tag{C 1}$$

for $z < z_J$, from (5.27b, c) and (5.31). The boundary condition as $z \to 0+$ is (5.28) while $\hat{U}_z = 0$ at the unknown $z = z_J$. For compactness, we let $F(X, z) = (\hat{U}/2a_2) - X$ and $\sigma(X, z) = (1-z)\ln(1-z)\hat{U}_z$, and introduce the junction-fitted coordinate $\eta = z/f$ so that

$$F_X = \frac{1}{f}\left(f'\eta F_\eta + \frac{\sigma\sigma_\eta}{1-\eta f}\right) \tag{C 2}$$

(where $'$ denotes differentiation with respect to X), subject to

$$F_\eta = 0 \text{ at } \eta = 1, \quad F_\eta \sim \frac{1}{2a_2\eta} \quad \text{as} \quad \eta \to 0+. \tag{C 3}$$

The first of these conditions requires $\sigma = 0$ at $\eta = 1$ such that $F_X = 0$ at $\eta = 1$ and thus $\hat{U}(z = f) = 2a_2X + c_1$. Since neglecting the outer part of model ensures that there is no significant variation in $\hat{U}$ between $z = f$ and the centreline $z = 1$, this gives the centreline velocity as $\hat{U}_{C_L} = 2a_2X + c_1$ for X of order unity. This linear growth rate is twice that of the corresponding result for the two-dimensional case.

The far-downstream position f_∞ of the junction is determined from the limit $X \to \infty$ in (C 2). Expecting $F_X = -1$ as $X \to \infty$, we consider $\sigma = f_\infty^{1/2}(\eta^2 f_\infty - 2\eta + d_1)^{1/2}$ for constant d_1. Since $\sigma \to -1$ as $\eta \to 0+$ from (C 3), $d_1 = f_\infty^{-1}$ and $\sigma = (\eta^2 f_\infty^2 - 2\eta f_\infty + 1)^{1/2}$. Finally, $\sigma = 0$ at $\eta = 1$ from (C 3) implies $(f_\infty - 1)^2 = 0$, giving $f_\infty = 1$.

The small-a_1 analysis thus shows that, after linear growth in the centreline velocity for X of order unity, a downstream state emerges where the centreline velocity

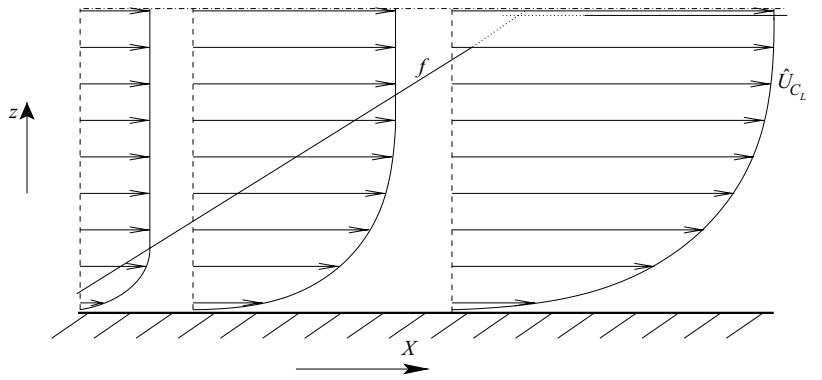

FIGURE 13. Predicted flow development from the small-a_1 analysis if $\hat{U}_X = 0$ downstream. This is a two-dimensional representation of the three-dimensional axisymmetric flow.

is constant and the junction position is constant and lies very near the centre-line. This is an approximation to its true position. We conclude that the three-dimensional axisymmetric case is in this way similar to the two-dimensional case; the flow development predicted here is shown in figure 13.

REFERENCES

BARBIN, A. R. & JONES, J. B. 1963 Turbulent flow in the inlet region of a smooth pipe. *Trans. ASME* D: *J. Basic Engng* **85**, 29–34.

BUSH, W. B. & FENDELL, F. E. 1972 Asymptotic analysis of turbulent channel and boundary-layer flow. *J. Fluid Mech.* **56**, 657–668.

CEBECI, T. & SMITH, A. M. O. 1974 *Analysis of Turbulent Boundary Layers*. Academic.

CHINNI, R., SAHAI, V. & MUNUKUTLA, S. 1996 Computational study of developing turbulent pipe flow. In *Hydrodynamics* (ed. A. T. Chwang, J. H. Lee & D. Leung). Balkema.

DEGANI, A. T., SMITH, F. T. & WALKER, J. D. A. 1993 The structure of a three-dimensional turbulent boundary layer. *J. Fluid Mech.* **250**, 43–68.

ELLIS, L. B. & JOUBERT, P. N. 1974 Turbulent shear flow in a curved duct. *J. Fluid Mech.* **62**, 65–84.

HUFFMAN, G. D. & BRADSHAW, P. 1972 A note on von Kármán's constant in low Reynolds number turbulent flow. *J. Fluid Mech.* **53**, 45–60.

HUNT, I. A. & JOUBERT, P. N. 1979 Effects of small streamline curvature on turbulent duct flow. *J. Fluid Mech.* **91**, 633–659.

KLEBANOFF, P. S. 1954 Characteristics of turbulence in a boundary layer with zero pressure gradient. *NACA TN* 3178.

KNIGHT, D. D. 1998 Inviscid compressible flow. In *The Handbook of Fluid Dynamics* (ed. R. W. Johnson). CRC.

LAUFER, J. 1949 Investigation of turbulent flow in a two-dimensional channel. *NACA Rep.* 1053.

LAUFER, J. 1952 The structure of turbulence in fully developed pipe flow. *NACA Rep.* 1174.

MAGER, A. 1964 Three-dimensional laminar boundary layers. In *Theory of Laminar Flows* (ed. F. K. Moore), *High Speed Aerodynamics and Jet Propulsion*, vol. 4. Oxford University Press.

MELLING, A. & WHITELAW, J. H. 1976 Turbulent flow in a rectangular duct. *J. Fluid Mech.* **78**, 289–315.

MELLOR, G. L. 1972 The large Reynolds number, asymptotic theory of turbulent boundary layers. *Intl J. Engng Sci.* **10**, 851–873.

NAKAO, S. 1986 Turbulent flow in square ducts after an expansion. *AIAA J.* **24** (6), 979–982.

NEISH, A. & SMITH, F. T. 1988 The turbulent boundary layer and wake of an aligned flat plate. *J. Engng Maths* **22**, 15–42.

NIKURADSE, J. 1933 Law of flow in rough pipes. *NACA TM* 1292.

Ockendon, H., Ockendon, J. R. & Falle, S. A. E. G. 2001 The turbulent boundary layer and wake of an aligned flat plate. *J. Fluid Mech.* **445**, 187–206.

Schlichting, H. & Gersten, K. 2000 *Boundary Layer Theory*, 8th edn. Springer.

Schwarz, W. R. & Bradshaw, P. 1994 Turbulence structural changes for a three-dimensional turbulent boundary layer in a 30° bend. *J. Fluid Mech.* **272**, 183–209.

Smith, F. T. & Li, L. 2002 Swirl flow effects in a duct bending through a substantial angle. *J. Engng Maths* **43**, 315–346.

Sychev, V. V. 1987 On turbulent boundary layer separation. In *Boundary Layer Separation* (ed. F. T. Smith & S. N. Brown). Springer.

Talbot, L. & Wong, S. J. 1982 A note on boundary-layer collision in a curved pipe. *J. Fluid Mech.* **122**, 505–510.

Wilson, P. L. 2003 On the core flow and turbulent boundary layer in a curved duct. PhD thesis, University of London.

Wilson, P. L. & Smith, F. T. 2005*a* A three-dimensional pipe flow adjusts smoothly to the sudden onset of a bend. *Phys. Fluids* **17**, 048102.

Wilson, P. L. & Smith, F. T. 2005*b* Compressible swirling flow through a significantly bent duct. *Comput. Fluids* **34**, 891–926.

Zhang, J. & Lakshminarayana, B. 1990 Computation and turbulence modeling for three-dimensional boundary layers including turbomachinery flows. *AIAA J.* **28**(11), 1861–1869.